The Cryosphere, 20, 6591–6611, 2026
https://doi.org/10.5194/tc-20-6591-2026
© Author(s) 2026. This work is distributed under
the Creative Commons Attribution 4.0 License.

The Cryosphere Open Access EGU

Linking ridge shapes to the ice thickness distribution via discrete element simulations

Marek Muchow[1,3], **Einar Ólason**[2], **and Arttu Polojärvi**[1]

[1]Aalto University, School of Engineering, Department of Mechanical Engineering, Espoo, Finland
[2]Nansen Environmental and Remote Sensing Center, Bergen, Norway
[3]Department of Physics and Technology, UiT The Arctic University of Norway, Tromsø, Norway

Correspondence: Marek Muchow (marek.e.muchow@uit.no)

Received: 22 December 2025 – Discussion started: 27 January 2026
Revised: 13 October 2026 – Accepted: 2 November 2026 – Published: 16 November 2026

Abstract. Sea-ice ridges are piles of ice rubble extending into the water and piling up on top of the ice, created by convergent ice motion. Consequently, ridges significantly increase the sea-ice thickness compared to the level ice surrounding them. In continuum sea-ice models, this increase is either represented by an increase in mean ice thickness or by changes in the ice thickness distribution (ITD). The implementation of ITDs requires a sub-grid parametrization of ridging by using a redistribution scheme. In contrast, the discrete element method (DEM) enables explicit simulations of the ridge-formation process, including ice fragmentation into rubble and its subsequent redistribution into ridges. Here, we use a DEM model to simulate ridging across a sea ice domain of size 6 km × 6 km. The DEM simulations yield deformed ice cover with ridges of varying shapes, namely triangular and trapezoidal ridges; the trapezoidal ridges notably affect the ITD of the deformed ice cover by creating a bump in the ITD towards thicker ice. We find that the ITD of the deformed ice field from DEM simulations differs from those from the continuum model, which uses only mean thickness, and from two commonly used ridging functions within redistribution schemes used as sub-grid parametrizations. Further, we show how to formulate an analytical redistribution function that captures the effect of various ridge shapes and discuss when it could replace existing ridging schemes. Our results suggest that a sub-grid representation of ridging is needed within continuum models to resolve ridges in both depth and shape within the ITD, especially in high spatial resolutions. Additionally, we discuss remaining challenges in implementing of our new distribution of ridged ice into continuum models, which relate to the ridging process itself.

1 Introduction

Ridges present localized discontinuities in the sea-ice cover by significantly increasing the ice thickness locally. They are formed due to convergent sea-ice motion creating deformation and failure of the ice. Consequently, ice blocks pile on top of the ice and under the water, respectively forming the ridge sail and keel, and thus, thickening the ice. Due to the thickening of the ice, ridging has a higher influence on the ice volume compared to its influence on the ice area (Mårtensson et al., 2012). For example, up to 36 % of the ice volume was consisted of thick ridges during MOSAiC from fall 2019 to late summer 2020 (von Albedyll et al., 2022). In turn, ridges also influence the sea-ice motion and deformation: The sail and keel influence the atmosphere and ocean drag, respectively, and the presence of ridges influences the large-scale ice-strength (Tuhkuri and Lensu, 2002; Martin et al., 2016; Tsamados et al., 2014; Brenner et al., 2021). Further, Krumpen et al. (2025) observed a rise in the annual number of ridging events due to an increase in first-year-ice fraction, indicating that ridging may become increasingly frequent and important in the future.

Despite their importance, the amount of thick and ridged ice is generally underestimated by conventional continuum sea-ice models (Johnson et al., 2012). Additionally, Bouchat et al. (2022) highlights that when comparing convergence from several models to satellite observations, only models running at a much higher resolution than the 10-km-resolution of the observed deformation fields were able to reproduce the observed convergence. As ridging requires convergent ice motion, the models may produce fewer ridges than expected. Further, Lipscomb et al. (2007) raised several

questions regarding the assumptions of currently used ridging parametrizations, for example, the shapes of participation and redistribution functions, which still remain open.

The representation of ridges in continuum models becomes even more important when they are adapted for high spatial and temporal resolutions, for example, for regional case studies, route planning, and operational forecast simulations (Blockley et al., 2020; Bouchat et al., 2022; Hutter et al., 2022; Williams et al., 2021). Especially for operational forecast simulations, the need for an accurate representation of ridges is emphasized, since ridged ice is one of the most common ice conditions where ships require icebreaker assistance and where winter navigation accidents occur (Valdez Banda et al., 2015; Liu et al., 2024).

Continuum sea-ice models describe ridging as a sub-grid process. They describe the ice thickness either by using a two-level approach (Hibler, 1979) that only includes an open-water fraction and a mean ice thickness (e.g., neXtSIM Ólason et al., 2022) or with a multi-category thickness (e.g., CICE Lipscomb et al., 2007; Hunke et al., 2010). In the first case, ridging increases the mean ice thickness, whereas in the latter one, ridging is described by sea-ice redistribution functions and the ice thickness distribution (ITD). The redistribution functions include a participation function that governs which part of the ice deforms and a ridging function that determines to which thickness category the deformed ice belongs. The two common ridging functions are either based on Hibler (1980), assuming triangular ridges and linear redistribution of ice, or Lipscomb et al. (2007), assuming an exponential distribution of smaller ridges compared to deeper ridges, reflecting observations (Wadhams, 1992; Amundrud et al., 2004; Rabenstein et al., 2010; von Albedyll et al., 2021).

In order to represent ridging more detailed than is possible in continuum models, we simulate ridging by using a three-dimensional discrete element method (DEM) model, which enables explicit simulations of ridge-formation processes. Three-dimensional simulations are required for realistic ridging simulations (Muchow and Polojärvi, 2024), compared to two-dimensional simulations of ridging, which reduce the ridge to its cross-section (Hopkins, 1994, 1998). Otherwise, two-dimensional DEM models often simulate ice floe interactions in the horizontal plane, which require the use of ridging parametrizations (e.g. Hopkins, 2004; Herman, 2016; Manucharyan and Montemuro, 2022; West et al., 2022). Contrary, in DEM simulations of ridge-formation processes, intact sea ice is modeled as particles connected by beams, which may fail and form ice blocks. The ridging is simulated explicitly, including ice rubble formation and ice rubble accumulation. The model we use is the Helsinki Discrete Element Model (HiDEM) (Åström, 2006), which has demonstrated its capability to simulate sea-ice dynamics and fragmentation in three dimensions over kilometer-scale domains at meter-scale resolution (Åström and Polojärvi, 2024; Åström et al., 2024). For example, Åström et al. (2024) compared sea-ice fragmentation simulations of the Kvarken area (Baltic Sea) to satellite images, with the model successfully replicating a significant portion of the fracture patterns, fast-ice distributions, and ice drift patterns. Further, they conducted simulations of ice compression in the Gulf of Riga showing a floe-size distribution and ridge development aligning with observations.

The results presented here provide insight into ridge shapes as well as their influence on the ITD of a deformed ice field. We compare the ITDs from our DEM simulations to those from commonly used sub-grid parametrizations in continuum models, namely ridging functions developed by Hibler (1980) (HI80) and Lipscomb et al. (2007) (LI07), and to the ITD resulting from the neXt-generation Sea Ice Model (neXtSIM) simulations. Here, neXtSIM represents a high-resolution continuum sea-ice model, where ice thickness within each grid cell is represented by its mean value only (Ólason et al., 2022). With these different models, we can compare results from explicit simulations that resolve the ridging process (DEM simulations) with those from commonly used methods in sea-ice continuum models, thereby shedding light on the ability of these methods to reproduce ITDs related to ridging. Such a direct comparison of simulations of sea-ice deformation from DEM and continuum models, which cover the same sea-ice area at similar spatial resolutions has not been previously presented. Our work demonstrates the potential of high-resolution sea-ice modeling using DEM and its complementary role relative to conventional large-scale sea-ice models.

Our high-resolution DEM simulations yield deformed ice covers with ridges of varying shapes, which we classify as triangular and trapezoidal ridges, as both are commonly observed keel shapes (Timco and Burden, 1997; Strub-Klein and Sudom, 2012; Eilers and Bradley, 2026). Once classified, the influence of the trapezoidal ridges on the ITD becomes evident. Notably, the effect of varying ridge shapes on ITD has not been included in any ice redistribution scheme, even if ridges occur in nature with varying shapes. We further develop an analytical description of the distribution of ridged ice that successfully incorporates the effect of ridge shapes and discuss when and how the introduced function could be used in ridging schemes in continuum sea-ice models.

In what follows, Sect. 2 first describes the general setup of our numerical experiments, followed by a description of HiDEM and neXtSIM models used and the sea-ice redistribution model implemented to account for sub-grid parameterizations of ridging. Section 3 presents our results, including a general description of the deformed ice fields yielded by different approaches. This section further shows how to derive an analytical description for the distribution of ridged ice accounting for different ridge shapes. Section 4 first discusses the influence of ridge shapes on the ITD as well as the differences in the ITD derived from HiDEM to field observations and second how ridging processes influence the ITD. This section also includes open questions regarding how to imple-

ment the derived distribution of ridged ice in redistribution schemes.

2 Methods

We use both discrete element and continuum methods to simulate sea ice ridging. To ensure comparability, the simulation setup introduced in Sect. 2.1 was adapted for each model. Next, Sect. 2.2 details the Helsinki Discrete Element Model (HiDEM), which simulates ridging at high spatial resolution. Results are then compared with those from the neXt-generation Sea Ice Model (neXtSIM), introduced in Sect. 2.3, and the sea-ice redistribution model, introduced in Sect. 2.4, which accounts for sub-grid parameterizations of ridging.

2.1 Simulation setup

Figure 1 describes the simulation setup with the main parameters summarized by Table 1. The simulations mimicked displacement-driven bi-axial compression tests, with constant velocities prescribed on the boundaries with constant y. Motion across the boundaries at $x = 0$ and $x = 6\,\mathrm{km}$ was restricted to prevent ice from drifting out of the domain. The domain size, $6\,\mathrm{km} \times 6\,\mathrm{km}$, was chosen large enough to fit several ridges while keeping the wall clock times for the simulations moderate. In addition, the chosen domain size was large enough to fit several grid cells of a high-resolution continuum sea-ice model.

All simulations start with a uniform ice thickness, but a non-uniform distribution of ice strength, as described below. The ice cover is then compressed over a period of two hours leading to a nominal strain of about 25 %. Simulations are conducted with three different initial ice thicknesses $h_\mathrm{i} = 0.5$, 1.0 and 2.0 m. This h_i range spans from thin ice up to the maximum thickness reached through thermodynamic growth (Maykut and Untersteiner, 1971). All simulations conducted with HiDEM and neXtSIM are repeated five times for each h_i. The ice thickness distributions (ITDs) presented in the results are averaged across the simulations with the same h_i. Appendix C gives the final deformed ice cover for each individual simulation and the respective ITD.

Comparing the model parameters influencing ice failure and ridging in HiDEM and neXtSIM is challenging as both models were developed for different applications and use different parameterizations. Nevertheless, both models have been successfully applied in modeling of sea-ice deformation. For example, Boutin et al. (2022) demonstrated neXtSIM's ability to reproduce Arctic sea-ice mass, while Åström et al. (2024) demonstrated HiDEM's ability to simulate sea-ice dynamics and fragmentation at meter-scale resolution over domains spanning tens of kilometers.

2.2 HiDEM

The Helsinki Discrete Element Model (HiDEM) describes the intact sea ice by using spherical particles connected by Euler-Bernoulli beams (Åström, 2006), which is rather standard for discrete element and bonded particle models (Cundall and Strack, 1979; Potyondy and Cundall, 2004). The motion of the particles is described by Newton's laws, with external forces applied to them due to elastic and inelastic contacts, buoyancy, gravity, drag, and friction. As the particles move, the beams deform. Upon reaching a predefined failure criterion, the beams fail, leading to ice failure and ice fragments of varying sizes. Here, a beam fails when its strain reaches a critical value, ϵ_c, defining the failure criterion. We selected $\epsilon_\mathrm{c} = 8 \cdot 10^{-5}$. Together with the chosen Young's modulus, $E = 4\,\mathrm{GPa}$, this gives a tensile strength of $\sigma_\mathrm{c} = 320\,\mathrm{kPa}$ according to Hooke's law ($\sigma_\mathrm{c} = E\epsilon_\mathrm{c}$). Both E and σ_c are within the range of engineering-scale sea ice properties (Timco and Weeks, 2010). Ridges form through the movement and accumulation of ice fragments formed by particles, thus, ridging is not explicitly parameterized in the model. More detailed information on HiDEM can be found in Åström et al. (2024).

The simulated ice cover was $6\,\mathrm{km} \times 8.2\,\mathrm{km}$ and had the ice with $y < 0$ and $y > 6\,\mathrm{km}$ constrained to move in the y-direction with velocities of 0.15 and $-0.15\,\mathrm{m\,s^{-1}}$, respectively (Fig. 1). Thus, undeformed ice was pushed with constant velocity into the observation area of $6\,\mathrm{km} \times 6\,\mathrm{km}$, after which the velocity of the particles is not controlled and allowed to change. We randomly removed beams bonding the particles to mimic the inhomogeneity of the ice cover and to introduce variation between simulation runs with the same h_i. This was done by splitting the initial ice cover into a $10\,\mathrm{m} \times 10\,\mathrm{m}$ grid, where each grid cell had a different, random value between 0.4 and 0.6 describing the number of beams present (beam probability). If the value was, for example, 0.55, then 55 % of the theoretical maximum amount of beams are present in this $10\,\mathrm{m} \times 10\,\mathrm{m}$ grid cell.

The simulation output was postprocessed into a gridded dataset with a resolution of $4h_\mathrm{i}$ to describe ice thickness at high spatial resolution, while ensuring that several discrete particles contribute to the ice thickness in each grid cell (see Appendix A).

2.3 neXtSIM

The neXt-generation Sea Ice Model (neXtSIM) was chosen as the continuum model, where the sea-ice cover is described with a brittle Bingham-Maxwell (BBM) rheology on a triangular, Lagrangian grid (Ólason et al., 2022). According to the comparison of several high-resolution models, neXtSIM fulfills the requirements to reproduce realistic linear kinematic features, which are bands of high deformation and thus, can be related to ridging (Hutter et al., 2022). The sea-ice thickness and changes due to deformation are represented with

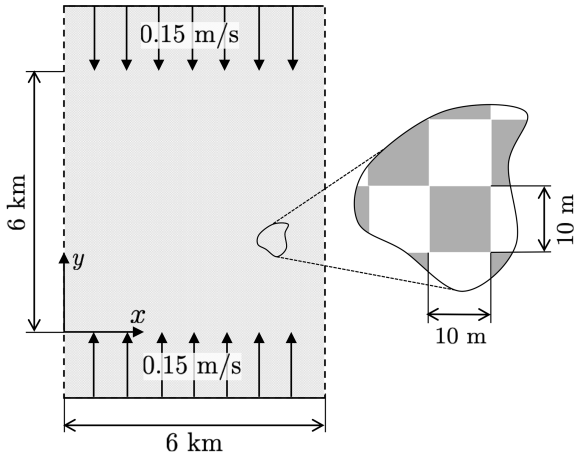


Figure 1. Description of the HiDEM simulation setup, also illustrating the overall simulation setup. The ice cover was split into a 10 m × 10 m grid shown in the closeup to implement the inhomogeneity of the ice with each 10 m × 10 m cell having a random beam probability between 0.4 and 0.6. A constant sea-ice velocity was applied so that level ice drifted into the observation area through the boundaries at $y = 0$ and $y = 6$ km, while ice drift across the boundaries indicated by dashed lines at $x = 0$ and $x = 6$ km was restricted. The area within the 6 km × 6 km is referred to as the observation area in the text.

Table 1. Main parameters of the HiDEM and neXtSIM simulations.

General Setup	Value	Unit
Initial ice thickness h_i	0.5, 1.0, 2.0	m
Ice Velocity	0.15	ms^{-1}
Simulation time t	2	h
Observation area	6×6	km^2
neXtSIM		
Mean edge length of the Lagrangian elements	100	m
Gridded sampling resolution	50	m
Output temporal resolution	30	min
Scaled cohesion	63	kPa
Young's modulus	0.6	GPa
Ridging threshold	10	kPa
HiDEM		
Gridded spatial resolution	$4h_i$	m
Output temporal resolution	20	min

one thickness value for each grid cell, representing the mean thickness for the area of that grid cell. During the simulations, the standard stand-alone variables, as presented in Ólason et al. (2022), are used and the sea-ice thermodynamics are turned off.

The BBM rheology is a damage propagation model (e.g. Girard et al., 2011; Amitrano et al., 1999) where the ice is modelled as a damaging elastic sheet. In this model, the elasticity is modulated by a damage variable, which is adjusted to reduce the elasticity whenever stresses in the model fall outside the Mohr-Coulomb envelope. The model also contains a viscous component to simulate stress relaxation after failure (Dansereau et al., 2016) and a friction element to prevent excessive ridging of damaged ice (Ólason et al., 2022). The cohesion of the Mohr-Coulomb envelope is a key parameter of this model, dictating the strength of intact ice. The cohesion scales with model resolution, so that the model can be run at different resolutions without adjusting this parameter. The effective cohesion in our case is $C = 63$ kPa. Other parameters, such as Young's modulus and the ridging threshold, are the same as in Ólason et al. (2022) and changing those has no qualitative impact on the results. With neXtSIM being a two-class model (ice and no ice), the ice thickness in it increases in convergence through conservation of volume and grid area, resulting in an increase in mean thickness.

To adapt neXtSIM to the idealized setup, ice gets generated at the boundaries, where the velocity is applied. Thus, throughout the whole simulation, ice with the initial ice thickness gets added into the simulation. To introduce variability between the simulations as well as a non-uniform ice strength, the cohesion is varied randomly in space between a maximum value and half of that maximum value following Dansereau et al. (2016).

Compared to the standard setting, the time step and spatial resolution are significantly increased. The main model time step, controlling the advection, is 1 s, with 240 sub-cycles used to solve the dynamics yielding in a dynamical time step of $1/240 \approx 0.004$ s. The spatial resolution of the simulation was 100 m for the triangular Lagrangian grid, resulting in gridded output with a spatial resolution of 50 m.

2.4 Sea-ice redistribution model

To complement the results from neXtSIM, we also use a simple sea-ice redistribution model describing the sub-grid parametrization of ridging within continuum models utilizing an ice thickness distribution (ITD). Thus, the ITD is given by $g(h)$ separating the ice within a grid cell in categories based on the ice thickness, h, and represents the amount of ice area and volume within each of these categories. Between each time step, the ice gets redistributed based on different redistribution schemes, consisting of a participation function and a ridging function.

Our sea-ice redistribution model is based on the implementation of the mechanical redistribution in ICEPACK (Hunke et al., 2024) and adapted to simulate sea-ice redistribution as a stand-alone model with two different ridging functions commonly implemented in large-scale sea-ice models. Thus, the ridging function is either based on Hibler (1980) (HI80), assuming a linear redistribution of ice based on the assumption of triangular ridges, or on Lipscomb et al. (2007) (LI07), assuming an exponential distribution of more smaller ridges compared to deeper ridges. Overall, the theory of the redistribution is based on Thorndike et al. (1975) and

Lipscomb et al. (2007) and explained in more detail in the Appendix B.

At the start of the simulation, all sea ice is within one ice category describing the initial thickness h_i as given in Table 1. During each time step, dt, we add the theoretical amount of ice area $\Delta = 2Lvdt$, with L the length of the observation area in the x-direction and v the ice velocity, to the ice thickness distribution $g(h)$ into the category of h_i. After that, we call the redistribution function Ψ. To ridge the whole amount of Δ, we need to apply Ψ several times until the sum of $A(h)$ is again 6 km × 6 km, as the ice area within HiDEM and neXtSIM is constant due to confinement. If Ψ is only applied once, the resulting area, as given by the sum of $A(h)$, is bigger than 6 km × 6 km as the amount of ice participating in the deformation is calculated from $g(h)$ by the weighting function $b(h)$ (Appendix B, Eq. B4). Further, the resulting area is also influenced by assumptions of the ridging functions. Additionally, our implementation assumes an ice concentration of 100 % rather than calculating opening/closing rates as well as additional advection. We used regularly spaced ice categories with lower boundaries ranging from 0.0 to 20 m with a spacing of 0.5 m, which covers the range of observed sea-ice thickness in the simulations conducted with HiDEM and neXtSIM. We used the redistribution model with a time step of 5 min to calculate $g(h)$ after 2 h.

Both ridging functions, HI80 and LI07, contain tunable parameters. For HI80, the main tunable parameter is the empirical thickness H_*, which directly influences the maximum depth of ridges via setting the upper limit of the ridging function to $2\sqrt{H_* h_i}$. H_* often ranges between 25 m, as used, for example, in ICEPACK, and 100 m, as proposed by Hibler (1980). These two different values for H_* either result in the maximum ridge depth to be $10h_i$ or $20h_i$, respectively. For LI07, e-folding scale of $\gamma(h_i, h)$ depends on the tunable parameter μ influencing the depth of ridges as well as the amount of smaller ridges present. For our initial simulations, H_* and μ are set according to the standard settings of ICEPACK (Hunke et al., 2024), $H_* = 25$ m and $\mu = 3\,\mathrm{m}^{1/2}$, both representing ice of about the same strength (Lipscomb et al., 2007). Further, we conduct sensitivity simulations where we vary H_* to 50 and 100 m, to include the value Hibler (1980) proposed, and μ to 4 and $6\,\mathrm{m}^{1/2}$, to include similar simulations with LI07.

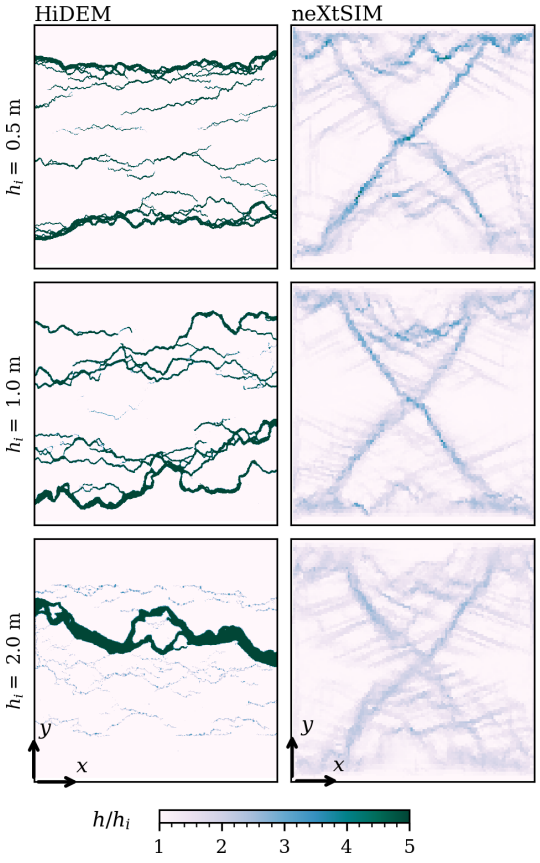


Figure 2. Ice thickness h normalized by the initial thickness h_i for each h_i (0.5, 1 and 2 m) and each model (HiDEM and neXtSIM) at the end of the simulations ($t = 2$ h). The domain size is 6 km × 6 km. The arrows in the bottom left corner indicate the coordinate system, with the convergent velocity applied in y-direction.

3 Results and analysis

3.1 Comparison of model results

Figure 2 illustrates the final deformed ice covers and differing ridge patterns in HiDEM and neXtSIM simulations. The ridges in HiDEM are mainly perpendicular to the direction of compression, whereas neXtSIM yields a dominant X-shaped ridge pattern accompanied by smaller ridges, consistent with the Mohr-Coulomb failure criterion implemented within its rheology. Nevertheless, thoroughly investigating the difference in spatial distribution between both would need simulations with more diverse forcing scenarios and, thus, is a task for further studies. Omitting the distribution of ridges, both HiDEM and neXtSIM contain ridges as localized features embedded in an undeformed ice. The ridges in HiDEM are more strongly localized, while ridges in neXtSIM appear more smudged over several grid cells. Furthermore, the ridges are significantly shallower in neXtSIM than in HiDEM.

To further investigate the ridges within HiDEM, we studied their cross-sectional keel shapes, a common method for classifying ridges based on observations (Timco and Burden, 1997; Strub-Klein and Sudom, 2012; Eilers and Bradley, 2026). The most common keel shapes are triangular and trapezoidal. Therefore, we identified ridges with a thickness of $> 3h_i$ along five transects at $x = 1.0$, 2.0, 3.0, 4.0 and 5.0 km at the end of the simulation and manually classified the shape of their cross-section into trapezoidal, triangular

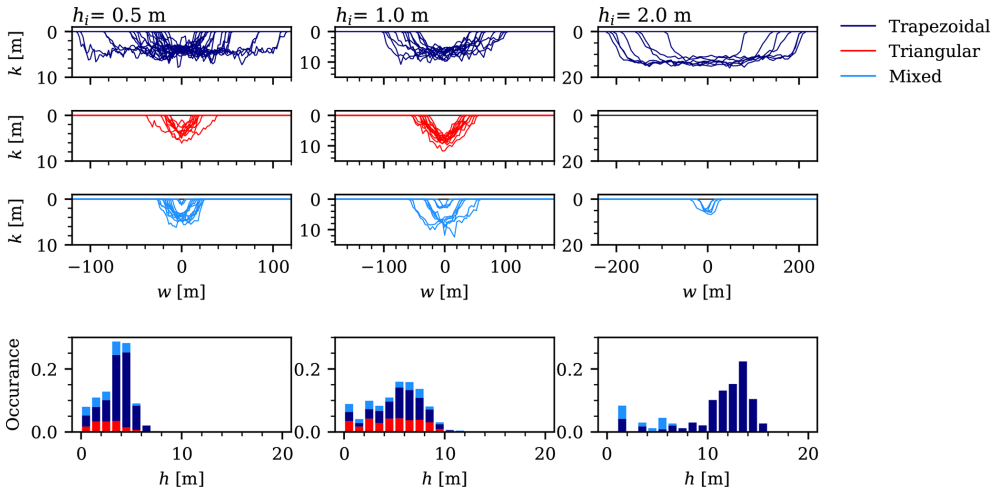


Figure 3. Ridge profiles are presented at the end of HiDEM simulations ($t = 2$ h) at five different cross-sections($x = 1.0$, 2.0, 3.0, 4.0 and 5.0 km) for all three initial ice thicknesses h_i. The ridge profiles were manually classified into trapezoidal, triangular and mixed shape as indicated by the legend colors. The shape was only defined for ridges of depth $> 3h_i$. The histograms in the bottom row show the contribution of each ridge type to the distribution of deformed ice per ice thickness categories h. Here, the distribution of deformed ice is given regarding the relative area coverage of each h. Note that the range of the axes for the ridge profile plots differs for each h_i.

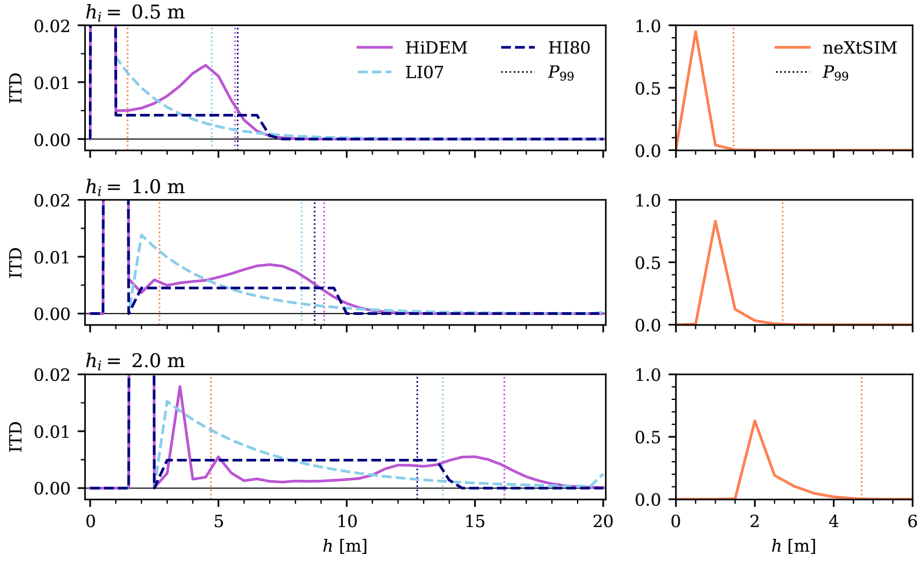


Figure 4. The ice thickness distribution (ITD) based on sea-ice area after $t = 2$ h. The results for HiDEM and the redistribution function utilizing two different ridging functions, LI07 and HI80 (Sect. 2.4), are shown in the left column, while the results for neXtSIM are shown in the right column. The dotted vertical line represents the upper 99th percentile P_{99}. P_{99} from neXtSIM is given in both columns to visualize that neXtSIM's ITD contains less thick ice. Note that the x and y axes ranges differ between the two columns. The ice thickness categories h are equally spaced categories form 0 to 20 m with a bin width of 0.5 m. The results of neXtSIM and HiDEM show the mean ITD and mean percentile across all five simulations.

and mixed as Fig. 3 shows. The mixed shape includes ridges very likely switching from triangular to trapezoidal shape as their shape is more round than triangular ridges, while not having an established plateau. The histograms in the bottom row of Fig. 3 show how ridges with each shape contribute to the area covered by each ice thickness category. While most of the ridges stemming from ice of $h_i = 0.5$ and 1.0 m are triangular (46 % and 39 %, respectively), the trapezoidal ridges (22 % and 33 %, respectively) are larger in size and consequently contribute more to the overall deformed ice both in area and volume. Similarly, for simulations with $h_i = 2.0$ m, about half of the ridges are rather large trapezoidal ridges, with the other half being small and of mixed shape; again, the trapezoidal ridges dominate the amount of deformed ice.

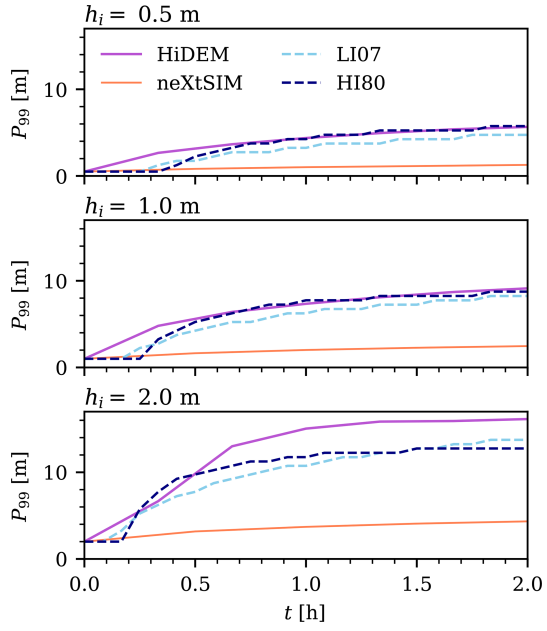


Figure 5. Development of the 99th percentile P_{99} of the ice thickness of the whole observation area (6 km × 6 km) is shown for HiDEM, neXtSIM, LI07 and HI80 for all three initial ice thicknesses h_i.

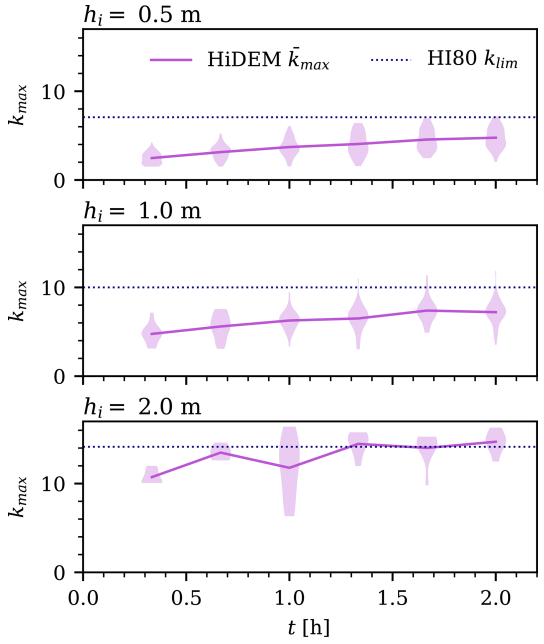


Figure 6. Evolution of the distribution of maximum keel depths k_{max} within HiDEM given as a violin plot for each time step for all three initial thicknesses h_i. For this purpose, ridges were identified along five different cross sections along the x-direction of the observation area, if $k_{max} \geq 3h_i$. The mean of k_{max}, $\bar{k}_{max}$, is given as solid line. The upper limit of the keel depths k_{lim}, as calculated by Hibler (1980) (HI80) with $H_* = 25$ m, is given as a dotted constant blue line.

Figure 4 shows the mean ice thickness distributions (ITD) calculated from the final deformed ice cover of all five simulations. The ITD associated with HiDEM features a bump, with its peak at ice thickness h, indicating the regime with the most of the deformed ice. This peak is around $h \approx 6h_i$, indicating a linear relationship between the h with most of the deformed ice volume and h_i. The histograms of Fig. 3 indicate that this bump is connected to the ice in trapezoidal ridges, while the plateau between h_i and the start of the bump is influenced by the ice in the triangular ridges. Additionally, the ITD for $h_i = 2$ m features a peak around 3 to 4 m, which is disregarded in the further analysis as it stems from rafting and results in an ice thickness below the criterion for ridges ($> 3h_i$).

Figure 4 also presents the final ITD for neXtSIM as well as those calculated by the sea-ice redistribution models with HI80 and LI07 ridging functions. For both neXtSIM and LI07, the ITD shows the largest amount of deformed ice near h_i, with a gradual decrease towards thicker ice. This decrease is significantly faster for neXtSIM compared to LI07, with the upper 99th percentile for neXtSIM being less than half of the 99th percentile for LI07 (dotted lines in Fig. 4). HI80 is, on the other hand, assumes that ridges are triangular. Thus, the ice redistribution is uniform between the rafting thickness and a set maximum ridge thickness (Appendix B). Consequently, the ITD is a flat line. Thus, neXtSIM and both redistribution functions, LI07 and HI80, create an ITD that differs from that given by HiDEM, due to both triangular and trapezoidal ridges.

Both HI80 and LI07 feature tunable parameters. As described in Sect. 2.4, we conducted sensitivity simulations within commonly used ranges of these parameters. For HI80, a lower H_* reduces the depth of ridges, and for, LI07 a smaller μ reduces the depth of ridges and results in a higher amount of smaller ridges. Nevertheless, these tunable parameters do not influence the general shape of the ITD.

While the shape of the ITDs showed significant differences, the development of the upper 99th percentile P_{99} of the ice thicknesses within the ITD aligns reasonably well between the sub-grid parametrizations and HiDEM simulations, as Fig. 5 illustrates. The magnitude and development of P_{99} for HiDEM is nearly identical to that for HI80 and LI07 for $h_i = 0.5$ and 1.0 m. For $h_i = 2.0$ m, HiDEM's P_{99} is about $2h_i$ higher than P_{99} given by HI80 and LI07. Additionally, the development of HiDEM's P_{99} shows a plateau, resulting from the increase in width of the trapezoidal ridges, which had an approximately equal depth (Fig. 3). Simultaneously, Fig. 3 also shows that neXtSIM significantly underestimates the depth of deformed ice compared to the other results. Thus, the comparison of P_{99} suggests that including a sub-grid parametrization of ridging supports the representation of deeper ridges compared to a two-level approach which only includes the mean ice thickness, as shown by neXtSIM.

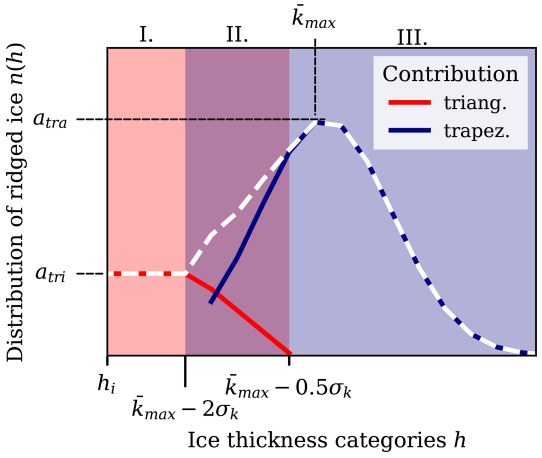


Figure 7. Sketch illustrating the derivation of the distribution of ridged ice $n(h)$ with the ice thickness categories h indication how much sea-ice area is covered by each category. Additionally, the contribution of the triangular and trapezoidal ridges is given in red and blue shading, respectively. $n(h)$ contains of three parts: Part I is influenced by triangular ridges only and Part III by trapezoidal ones, while Part II describes the transition between them. The input parameters of $n(h)$ are the mean maximum keel depth $\overline{k}_{\max}$ and its standard deviation σ_k, and a_{tri} and a_{tra} regulating the contribution of the triangular and trapezoidal ridges, respectively. All input parameters are annotated in the sketch.

3.2 Distribution of ridged ice $n(h)$

Here, we introduce a new function describing the distribution of ridged ice $n(h)$, based on the influence of the ridge shape on the ITD (Fig. 3). Conceptually, this function accounts for triangular ridges, similar to Hibler (1980), but extends it to include trapezoidal ridges. Thus, one input parameter of $n(h)$ is based on the maximum depth of ridges $k_{\max}$. Figure 6 presents the evolution of the distribution of $k_{\max}$ in HiDEM as well as the mean of $k_{\max}$ given as $\overline{k}_{\max}$. At $t = 2\,\text{h}$, $\overline{k}_{\max}$ is approximately constant for $h_{\text{i}} = 0.5\,\text{m}$ and $h_{\text{i}} = 2.0\,\text{m}$ and the distribution of $k_{\max}$ seems to only show minor changes for $h_{\text{i}} = 1.0\,\text{m}$. To simplify this derivation, we treated the entire simulation time $t = 2\,\text{h}$ as a single time step, which allowed us to treat $\overline{k}_{\max}$ as a constant. Thus, the used values for $\overline{k}_{\max}$ and its standard deviation σ_k are their values at $t = 2\,\text{h}$.

First, we propose splitting the ITD $g(h) = d(h) + u(h)$ with an ITD for deformed ice $d(h)$ and undeformed $u(h)$, meaning thermodynamically grown ice. Thus, during redistribution ice will be removed from $u(h)$ and added to $d(h)$ based on the newly calculated $n(h)$. This split has already proven to be useful to analyze sub-grid processes by Flato and Hibler (1995), as $d(h)$ offers detailed information on the properties of the ridges within one grid cell.

To describe the ridged ice $n(h)$, the function is split into three different parts describing different ridge shapes as illustrated in Fig. 7. First, the plateau of Part I, having the amplitude a_{tri}, describes the contribution of triangular ridges. Part III describes the trapezoidal ridges using a Gaussian curve with the maximum value a_{tra} giving the amplitude of the Gaussian curve. Part II describes the transition between the two and comprises of a linear function decreasing from a_{tri} to zero, as well as the same Gaussian curve as Part III. Thus,

$$n(h) = \begin{cases} a_{\text{tri}}, & \text{Part I} \\ a_{\text{tri}} \left(1 + \frac{\overline{k}_{\max} - 2\sigma_k}{1.5\sigma_k}\right) - \frac{a_{\text{tri}}}{1.5\sigma_k} h + a_{\text{tra}} \exp\left(-\frac{(h-\overline{k}_{\max})^2}{2\sigma_k^2}\right), & \text{Part II} \\ a_{\text{tra}} \exp\left(-\frac{(h-\overline{k}_{\max})^2}{2\sigma_k^2}\right), & \text{Part III.} \end{cases} \quad (1)$$

Part I is calculated for h between $h_{\text{i}} \leq h < \overline{k}_{\max} - 2\sigma_k$. The upper boundary of Part I also defines the lower boundary of the Gaussian function influencing Part II and III. Per definition of a Gaussian normal distribution, around 97 % of the distribution is accounted for above $\mu - 2\sigma$, with μ and σ being the mean and standard deviation of the distribution. Thus, the limit of $\overline{k}_{\max} - 2\sigma_k$ is set so that most of the Gaussian function is included in $n(h)$. Part II is then calculated between $\overline{k}_{\max} - 2\sigma_k \leq h < \overline{k}_{\max} - 0.5\sigma_k$, where the upper boundary was chosen ad hoc so that the transition between Part II and Part III is smooth. a_{tri} and a_{tra} are the amplitudes of the triangular and trapezoidal contribution to $n(h)$. Equation (1) presents $n(h)$ with respect to the sea-ice area. Thus, $n(h)$ can then be used to calculate the ridged ice with respect to volume $n_V(h)$ as follows: $n_V(h) = n(h)h$.

The main step to calculate $n(h)$ according to Eq. (1) is to calculate both a_{tri} and a_{tra}. Therefore, we rely on the ITD describing the distribution of the deformed-ice area to determine the sum of deformed area A_{d}, which gets updated by the amount of ice to be deformed during the current time step. Additionally, we introduce $\alpha = A_{\text{tri}}/A_{\text{tra}}$, with A_{tri} and A_{tra} being the areas of A_{d} influenced by triangular and trapezoidal ridges. Using this relationship, we can connect A_{d} with a_{tri} and a_{tra}. Thus, α gives the relationship between triangular to trapezoidal ridges and can be seen as an initially-set tuning parameter. Overall, a higher α results in a less pronounced bump, signaling more trapezoidal ridges. The detailed derivation of $n(h)$ is given in the Appendix D, while the steps can be summarized as follows: First, a_{tri} is calculated based on A_{d}, $\overline{k}_{\max}$, σ_k, h_{i} and α (Eq. D12). Second, a_{tra} is calculated based on a_{tri} and $\overline{k}_{\max}$, σ_k, h_{i} and α (Eq. D11). In the last step $n(h)$ is updated based on Eq. (1) as all needed input parameters are available. Overall, $\overline{k}_{\max}$ and σ_k could also be derived from observations.

We used two approaches to estimate $\overline{k}_{\max}$ and σ_k. First, we estimate $\overline{k}_{\max}$ and σ_k from HiDEM data. Therefore, we sample $k_{\max}$ for each ridge with $k_{\max} \geq 4h_{\text{i}}$ to exclude small and underdeveloped ridges at $t = 2\,\text{h}$. The mean and standard deviation of this dataset corresponds to $\overline{k}_{\max}$, as shown in Fig. 6, and σ_k, respectively. While $\overline{k}_{\max}$ increases with h_{i}

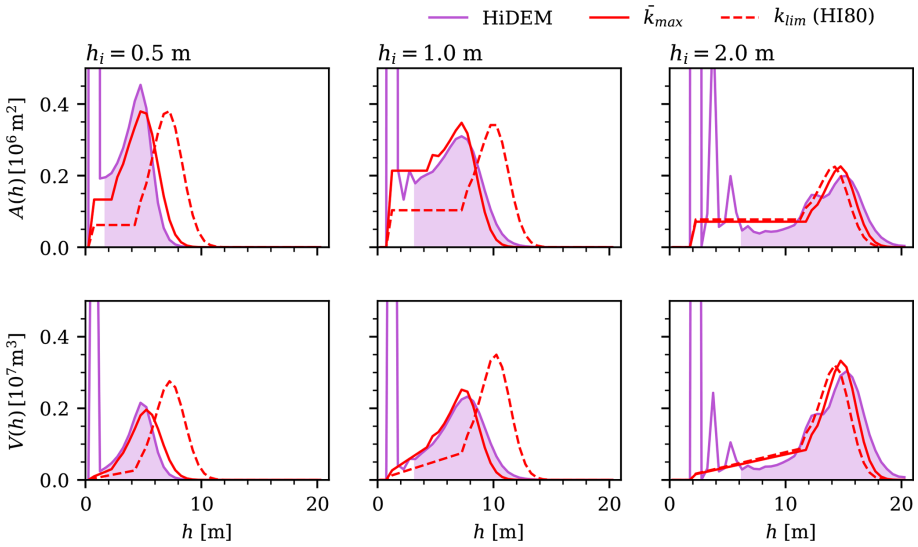


Figure 8. Results of the distribution of ridged ice $n(h)$ (Eq. 1) compared against the HiDEM's ITD after t =2 h, with the deformed ice $d(h)$ as $3h_i \leq h$ being highlighted by the pink shading. $n(h)$ was calculated either with the mean maximum keel depth $\overline{k}_{\max}$ and its standard deviation σ_k calculated based on HiDEM data (solid line) or with $\overline{k}_{\max}$ based on Hibler (1979) and σ_k being the mean value of σ_k from HiDEM data (dashed line).

(5.0 m, 7.2 m and 14.7 m for $h_i = 0.5$, 1.0 and 2.0 m), the values for σ_k are relatively similar to each other, which is why we use the mean of σ_k ($\overline{\sigma}_k = 1.28$ m) for each h_i. Second, we calculate $\overline{k}_{\max}$ based on the upper limit for the HI80 redistribution $k_{\lim} = 2\sqrt{H_* h_i}$ with $H_* = 25$ m, shown as the blue dotted line in Fig. 6, and use $\overline{\sigma}_k$ from HiDEM data. The tuning parameter α was selected through visual comparison of the calculated $n(h)$ with HiDEM's ITD, choosing the value that yielded the closest overall agreement ($\alpha = 0.2$, 0.5 and 0.7 for $h_i = 0.5$, 1.0 and 2.0 m, respectively). Both versions of the redistribution of ridged ice $n_A(h)$ and $n_V(h)$ are shown together with $g_A(h)$ and $g_V(h)$ yielded by HiDEM in Fig. 8.

Overall, the shape of $n(h)$ is consistent with the results from HiDEM (Fig. 8). Estimating $\overline{k}_{\max}$ and σ_k from HiDEM results in a closer fit than using the HI80 approach. The different phases of $n(h)$ (Eq. 1) successfully reproduce the plateau towards thinner ice as well as the bump towards thicker ice. Only very small differences are observed in the location of the peak between $n(h)$, calculated based on $\overline{k}_{\max}$ derived from the ridges in HiDEM, compared to the ITD derived from HiDEM data directly. Calculating $\overline{k}_{\max}$ based on $k_{\lim}$ (HI80) overestimates the location of the peak significantly for for $h_i = 0.5$ and 1.0 m resulting in too much deformed ice, while the difference for $h_i = 2.0$ m is significantly smaller. This observation suggests that this calculation method might not be suitable for estimating $\overline{k}_{\max}$ (Fig. 8). Contrary to $k_{\max}$ based on HI80, $\overline{k}_{\max}$ derived from HiDEM seems to follow a linear relationship with h_i at $t = 2$ h. It should be noted that $k_{\lim}$ was derived to estimate the overall upper limit of the distribution and not a mean distribution of maximum keel depths. Thus, while the derived function to describe ridged ice $n(h)$ captures the ITD from HiDEM, for larger-scale applications, it is important to select the input variables carefully.

4 Discussion

4.1 Simulation setup

Here, the forcing in the ridging simulations corresponds to uniaxial compression. Nevertheless, the ice within the 6 km × 6 km domain can theoretically fail both in shear and in compression. The predominant ridge pattern in neXtSIM (Fig. 2) demonstrates shear failure, which can be explained by the use of the Mohr-Coulomb failure criterion. Generally, this failure criterion seems to be favorable for continuum models to create intersection angles similar to those observed in nature compared to an elliptical yield curve (Ringeisen et al., 2019). A more complex forcing in neXtSIM could likely yield a different ridge pattern, but the failure mode that creates the ridges would remain similar. It is also unlikely that a different forcing of similar magnitude would produce significantly deeper ridges. Additionally, the ITD is also influenced by the absence of a sub-grid parametrization. Consequently, we assume that the resulting ITD would be similar.

Contrary to neXtSIM, the failure pattern in HiDEM shows ridges mainly perpendicular to the direction of compression. This difference may be related to HiDEM's simple local failure criterion: a beam breaks once its strain exceeds a fixed threshold, whether the deformation is tensile, shear or mixed mode (Sect. 2.2). The potential influence of the failure criterion can be illustrated by comparing the ridge pattern of

HiDEM to the pattern of ice floes created under uniaxial compression by Wilchinsky et al. (2010). They used a two-dimensional model with a Mohr-Coulomb failure criterion describing the local failure to simulate failure of bonded ice floes having an average floe size of 4 km. The resulting floe pattern depended strongly on the ratio of tensile to compressive strength: When the tensile strength is significantly lower than the compressive strength, diamond-shaped floes form, while failure between floes becomes increasingly perpendicular to the forcing direction with the ratio of tensile to compressive strength increasing. This suggests that our failure pattern in HiDEM could, at least in part, be related to having a simple failure criterion, which does not account for compressive failure of the beams. However, a closer inspection of HiDEM results shows that several individual ridges for $h_\mathrm{i} = 0.5$ and 1.0 m are connected, featuring varying intersection angles and floe shapes (Fig. 2). As these simulations feature idealized forcing and simulation domain, we do not directly compare the simulated ridge pattern or intersection angles with observations. Nevertheless, Åström et al. (2024) demonstrated HiDEM's ability to reproduce failure patterns observed in the Baltic Sea using forcing that varied in time. Additionally, simulations of fragmentation of ice blocks showed that the macroscale ice failure resulting from HiDEM can be described by Mohr-Coulomb criterion (Prasanna et al., 2022). Thus, the ridge pattern is likely not only influenced by the failure criterion, but also by the applied forcing. More diverse forcing or a more complex failure criterion could result in a more diverse ridge pattern.

A different forcing scenario likely results in different locations of beam failure in HiDEM, which in turn influences the location of the ridges. While it is out of the scope of this study to investigate the exact effect of various forcing scenarios on the ridge shapes, we argue that the creation of trapezoidal ridges is still likely. If the amount of ice to be redistributed is the same and the number of ridges is similar (as the local failure criterion stays the same), the ice volume to be redistributed into these ridges is similar, which would then still create trapezoidal ridges. Nevertheless, further work on the influence of forcing scenarios on the resulting ridge shapes and ITD are still required.

Because HiDEM is a discrete-element model, we must regrid particle positions onto a fixed-resolution grid to derive the local ice thickness from which we can calculate the ITD (Appendix A). The resolution of this fixed grid, dx, can be related to the initial ice thickness, h_i, or some fixed reference. To assess the influence of dx on the derived ITD, we regridded the HiDEM output to the same resolution as neXtSIM ($dx = 50$ m) and compared this to the original ITD obtained by relating dx to the initial ice thickness via $dx = 4h_\mathrm{i}$. Interestingly, the ITD shape derived from the coarser spatial grid significantly changes for $h_\mathrm{i} = 0.5$ m and 1.0 m compared to the original ITD (Fig. 9). This ITD declines gradually from thinner ice to thicker ice and is closer in shape to the results from LI07 and neXtSIM than HiDEM's ITD at $dx = 4h_\mathrm{i}$.

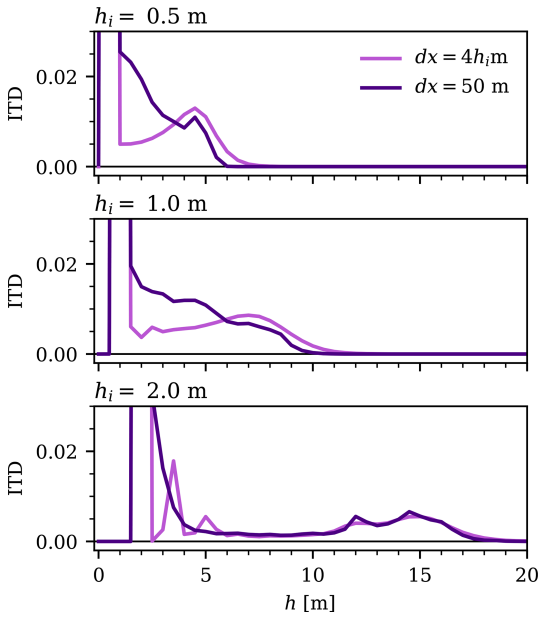


Figure 9. The ITD from the final deformed ice cover ($t = 2$ h) from HiDEM for two different spatial resolutions dx for each initial ice thickness h_i (0.5, 1 and 2 m).

Thus, the spatial resolution of the regridded thickness field can influence the shape of the derived ITD.

The role of regridding or sampling resolution can be explained by how sampling affects the resolved ridge width. The width of the triangular and mixed ridges is between 20 and 80 m for $h_\mathrm{i} = 0.5$ m, and 20 and 120 m for $h_\mathrm{i} = 1.0$ m (Fig. 3). With coarse sampling ($dx = 50$ m), a substantial fraction of grid cells will contain a mixture of deformed and undeformed ice, resulting in a thinner mean ice thickness. Consequently, the derived ITD then contains more ice in categories representing thinner ice, as shown in Fig. 9. The differences between the ITDs for $h_\mathrm{i} = 0.5$ and $h_\mathrm{i} = 1.0$ m are largest between the level ice and the peak of the bump, which covers the contribution of triangular ridges (Fig. 7). In contrast, most trapezoidal ridges are significantly wider than the coarser sampling resolution, so the ITD shows fewer changes in the contribution of trapezoidal ridges and depends less on dx for $h_\mathrm{i} = 2.0$ m. This comparison implies that ice thickness must be sampled carefully when deriving ITD parametrizations so that ridge depth is appropriately represented.

4.2 Ridge distribution

Although the spatial distribution of the ridges between both HiDEM and neXtSIM is significantly different (Fig. 2), both distributions contain features present in observations. The ridge pattern in neXtSIM is reminiscent of the patterns seen in similar experiments with the viscous-plastic rheology (e.g., Ringeisen et al., 2023). Additionally, ridges in observational datasets are often identified by either a minimum thick-

ness or an increase in thickness compared to the surrounding ice (e.g. Duncan and Farrell, 2022), meaning that ridges should appear as localized features within the ice cover.

We investigated the number of ridges within the 6 km × 6 km domain in HiDEM simulations by counting ridges along five transects at $x = 1.0, 2.0, 3.0, 4.0$ and 5.0 km. Therefore, a ridge was identified as a ridge if the keel depth was at least 1.5 times deeper than the initial ice thickness h_i (or $2.0h_\mathrm{i}$, $2.5h_\mathrm{i}$ and $3.0h_\mathrm{i}$). Overall, the number of ridges decreased with increasing h_i in our HiDEM simulations. This observation is intuitive, as the characteristic length L_C for a beam or plate on an elastic foundation is proportional to the ice thickness ($L_\mathrm{C} \propto h^{3/4}$) (Hetenyi, 1946). L_C is related to the failure length of such a beam or plate under bending; for a given area of ice cover, thin ice is expected to fail more frequently than thick ice. L_C is often used to assess the length scale for ice failure (Sanderson, 1988; Hopkins, 1998; Amundrud et al., 2004). Analogously, field observations analyzed by Uusinoka et al. (2025a) suggest that thin ice yields spatially more frequent deformation features than thick ice, whereas the deformation features with thick ice are more prominent and Krumpen et al. (2025) observed more ridging events across the Arctic covered by thinner ice compared to thicker ice. Both of these observations align with those related to the ridging in HiDEM simulations.

4.3 Ridge shapes and ITD

Field observations have shown that the shapes of ridges show large variability, with triangular shapes often assumed for first-year ridges and trapezoidal shapes for multi-year ridges (Timco and Burden, 1997; Strub-Klein and Sudom, 2012). Additionally, Eilers and Bradley (2026) summarized the shape of keels based on different observational studies since the 1970s. The keel shape was described as triangular, trapezoidal, rectangular, or having concave or elliptical forms, with triangular and trapezoidal shapes being the most common keel shapes. Thus, the keel shapes produced by HiDEM simulations are within the expected ranges from observations. Further, Eilers and Bradley (2026) revisited submarine sonar data from the Arctic Ocean between 1960 and 2005 to analyze the shape of over 600 000 keels. They found that the shape of the keel cross-section for keels between 2 and 8 m depth was mainly trapezoidal (88 %), while ridges between 8 and 12 m depth demonstrated triangular shapes as the most common keel shape. In HiDEM, all keels for $h_\mathrm{i} = 0.5$ m and most of the keels for $h_\mathrm{i} = 1.0$ m are below 8 m depth (Fig. 3) with 22 % and 33 % of the ridges being trapezoidal. Although our percentages are considerably lower, the analysis by Eilers and Bradley (2026) highlights the importance of accounting for both ridge shapes.

Commonly used ridging functions do not capture the ITD of the deformed ice cover produced by HiDEM (Fig. 4). This discrepancy is due to the ridges of trapezoidal shape, which yield a bump in the ITD around the thickness h representing the keel depth. Previous two-dimensional DEM simulations of the formation of individual ridges similarly yielded trapezoidal ridge shapes that had a similar effect on the ITD (Hopkins, 1996, 1998). Our findings, importantly, extend these results by confirming that trapezoidal ridges have a significant effect on the ITD for a deformed ice cover, which contain multiple ridges. While the relative number of trapezoidal ridges increases with h_i, their influence on the ITD is significant for the thinnest ice tested here as well as they cover a large area of sea ice and contain a large amount of sea-ice volume. Thus, even with the ice cover thinning due to climate warming and simultaneously the number of ridging events increasing (Krumpen et al., 2025), ridging schemes should account for various ridge shapes.

ITDs are generally formulated based on observations on the distribution of ridge keels (Wadhams, 1992; Melling and Riedel, 1996; Amundrud et al., 2004; Yu et al., 2004; Metzger et al., 2021), the distribution of sails via surface elevation (Petty et al., 2016), via electro-magnetic measurements of the whole ice thickness (Haas et al., 2009; Rabenstein et al., 2010) or by using a combination of these methods (Haas et al., 2008). These studies led to ITDs with a long tail representing ridges, which is often described by a negative exponential function (Amundrud et al., 2004; Rabenstein et al., 2010; von Albedyll et al., 2021). This differs from the shape of the ITDs derived from HiDEM. All of the aforementioned observations are conducted over larger areas with more variations in the ice conditions, for example thickness and ice motion, than the here used observation area. Additionally, they reflect ice deformation that has occurred in multiple stages over longer periods. Often, these observations are based on measurements of the sail, which require assumptions of the keels underneath the water, which further complicates a direct comparison. Hopkins (1996) suggested that the negative exponential form stems from thickness contributions of multiple ridges in various stages of development superposed; the negative exponential form may consist of several bumps combined into one curve.

Sumata et al. (2023) presents ITDs with a second modal peak having a very similar shape as the bump observed in HiDEM's ITD, which adds observational support to the overall shape of the ITD. This peak describes ice from the Arctic Basin being transported through the Fram Straight, which likely has experienced several deformation events and thus contains ridges. Overall, the location of the peak is at thinner ice thicknesses, which could also be explained by melting of the ridges, while being transported. Further, in von Albedyll et al. (2021), an ITD calculated over fast ice contains a bump between 3.0 and 3.5 m and a bump around 2.5 m with a plateau leading up to it. Assuming that fast ice has a more uniform thermodynamically-grown thickness, this observation supports our observation of an ITD containing a bump to describe ridges.

To date, the only link between ridge shapes to negative-exponential tail of the ITD is based on the assumption that

an average ridge has a cusp shape (Amundrud et al., 2004). This average ridge shape has been observed by Metzger et al. (2021) analyzing underwater keel measurements. They argue that the cusp shape is a result of shearing. The assumption on such shape contradicts current understanding of how ridges form as demonstrated by direct field observations and numerical simulations.

Overall, there is a need for more detailed observations on the connection of ridges and the ITD. Field observations on ridges, and especially their shape, are very laborious and often limited to a smaller domain. Additionally, most ridge and ITD observations are instantaneous instead of observing the evolution of a specific sea-ice area. Combining observations of changes in the ITD, similar to the approach of von Albedyll et al. (2022), with observations of ridge shapes or volume of ridged ice over the same time period would likely answer several open questions about the contribution of ridging to the ITD.

4.4 Ridging processes and ITD

The derivation of the proposed distribution of ridged ice $n(h)$ (Eq. 1) leaves two main questions to be addressed for its implementation into a continuum sea-ice model: (1) how do $\overline{k}_{\max}$, σ_k and α depend on the deformation history of a grid cell or can they be assumed constant and (2) what is the process scale to calculate volume of deformed ice V_d? Once these questions are answered, $n(h)$ could replace the ridging function $\gamma(h_\mathrm{i}, h)$ in redistribution schemes. Overall, they relate to open questions regarding the understanding of ridging processes and are explored next.

Current ridging functions, like that of H80, assume a global limit for the ridge depth, k_lim, and ignore a potential development of the maximum depth of each ridge k_max during deformation. While we observe variation between the individual ridge depths yielded by HiDEM, the mean of the maximum keel depths $\overline{k}_{\max}$ reaches a constant value, as the ridges start growing in width and transfer towards trapezoidal shape (Figs. 3 and 6). Additionally, σ_k shows no significant variation with h_i and can be assumed constant. Thus, we propose using a $\overline{k}_{\max}$ that increases linearly with h_i. Nevertheless, a more sophisticated implementation of $\overline{k}_{\max}$ could depend on the available forcing during a deformation event, as proposed by a folding rate of the ITD proportional to the deformation rate (von Albedyll et al., 2021) and the available ice (Amundrud et al., 2004).

Most observations have focused on finding k_lim instead of the distribution of k_max via $\overline{k}_{\max}$ and σ_k. Using $\overline{k}_{\max}$ instead of k_lim within our ridging function accounts for the fact that several ridges may not reach k_lim, due to either the surrounding ice thermodynamically having thickened since the ridge building, the keel melting, or all available ice having been incorporated into the ridge (Amundrud et al., 2004). Based on observations, Amundrud et al. (2004) found a k_lim of $20\sqrt{h_\mathrm{i}}$ with is equal to Hibler (1980) with a $H_* = 100\,\mathrm{m}$. This limit is significantly higher than the HI80 k_lim calculated with $H_* = 25\,\mathrm{m}$, as used in this study and in ICEPACK. Further, HI80 k_lim is a close upper bound to the distribution of k_max in HiDEM (Fig. 6).

Deriving a relationship for α depends on, for example, the number of ridges in a grid cell or the severity of ice deformation. Our results suggest that a relationship for α must account for the ice thickness, but α could also be connected to the large-scale ice strength or to the severity of deformations. Values or functions for α could be determined by comparing results from a sea-ice model utilizing the suggested scheme with observations or by using results from DEM simulations with diverse forcing scenarios and varying initial ITDs.

The calculation period of the volume of deformed ice V_d needs to have a defined start and end point within the redistribution scheme. Deformation events, and thus ridging, seem to have a temporal scale of several hours (von Albedyll et al., 2022), which would indicate calculating V_d over the scale of a deformation event. Instead of using the length of a deformation event as the period over which V_d accumulates, the period may also be limited by the consolidation time of the formed ridges, as the initial consolidation occurs over a period varying from hours to days, depending on the initial ice thickness and surrounding conditions (Maus, 2025). To account for ridge consolidation, the model by Salganik et al. (2020) could be used. However, it is unclear whether ridges grow only during a single deformation event or whether subsequent events continue to grow the same ridges rather than establish new ones.

The following examples highlight how the implementation of $n(h)$ and its requirements may benefit other areas of sea-ice dynamics within continuum sea-ice models. First, the split of $g(h)$ into $d(h)$ and $u(h)$ consequently requires a reformulation of the participation function $a(h)$ (Eq. B3 in Appendix B) to only allow undeformed ice to get deformed, $a(h) = b(h)u(h)$. This reformulation improves the physical meaning of the function, as it accounts for ridges only consisting of broken-off ice blocks from the surrounding level ice (Strub-Klein and Sudom, 2012; Kulyakhtin and Høyland, 2014). Second, having a separate distribution for deformed ice via $d(h)$ allows us to account for macroporosity in ridges, with, for example, either a mean macroporosity or parameterizations like the one proposed by Maus (2025). Currently, redistribution functions do not account for macroporosity within ridges, except for the scheme proposed in Roberts et al. (2019). Third, ridge-grounding schemes could be directly connected to results from redistribution, as Dupont et al. (2022) argued that high fractions of likely undeformed thin ice within $g(h)$ influenced their calculation of the maximum keel depth and thus the grounding of ridges. These ridges are important for the representation of landfast ice (e.g. Mahoney et al., 2007).

With the split of $g(h)$, it is possible to create ice categories suitable for both thermodynamics and redistribution of ice. Currently used ranges better resolve thinner ice. For exam-

ple, the lower bounds of the ice categories for ICEPACK (original setting) are 0, 0.64, 1.39, 2.47, and 4.57 m (Hunke et al., 2024). These ranges highlight that current implementations of the ITD focus on the representation of thin ice, as it has a stronger effect on thermodynamics, whereas a significant fraction of ridged ice falls within a single ice category. To circumvent the influence of the split of $g(h)$ on other parametrizations, like the floe-size distribution, $g(h)$ can always be easily calculated from $g(h) = u(h) + d(h)$. Nevertheless, the split of $g(h)$ would also increase model complexity with potential impacts on the performance of the model. The balance of the right amount of complexity needs to be decided based on the application and user of the model (Blockley et al., 2020).

As described above, implementing $n(h)$ in a continuum sea-ice model is not straightforward and requires additional decisions regarding sea-ice redistribution schemes. We developed $n(h)$ because none of the established ridging functions, HI80 and LI07, reproduced the shape of HiDEM's ITD. The ridging function based on HI80 accounts only for triangular ridges, while LI07 is based on observations over larger areas of the deformed ice cover. Thus, $n(h)$ follows a different approach than LI07 by accounting for different ridge shapes and indirectly connecting the ITD to the ridging process. Further, it can be seen as an extension of HI80.

Overall, the spatial comparison of HiDEM and neXtSIM and the comparison of the ITDs yielded by them implies that only increasing the spatial resolution of continuum models, within the limits of their practical use, is not sufficient to improve the representation of ridges as localized features within the ice cover featuring a depth comparable to observations. This observation aligns with results from a comparative study by Hutter et al. (2022). In their case, the limit was related to the tendency of high-resolution continuum simulations to produce leads rather than ridges. Further, the comparison of the ITD from neXtSIM to the ITDs from both redistribution functions indicates that including sub-grid parametrizations improves the representation of deeper ridges. Additional limits to the applicability of continuum models in high-resolution modeling are set by the minimum domain size for observing scale invariance and multifractal behavior of sea ice (Uusinoka et al., 2025a, b). Thus, representing ridging even in high-resolution continuum models will require suitable sub-grid parametrizations of ridging as well as the connection of ridging to the large-scale ice strength. To this end, as also demonstrated here, DEM models are a suitable tool to complement continuum models in detailed investigations on sea-ice deformation.

5 Conclusions

We conducted high-resolution simulations to study how the ridge shape influences the ice thickness distribution (ITD) by using a three-dimensional discrete element model, HiDEM, which enabled us to simulate ice failure and ridge-formation processes explicitly. Further, we compared these results to those from neXtSIM, a continuum model representing the ice thickness by the mean thickness, and to two commonly employed redistribution schemes in sea-ice models using ITD, with the ridging function based on Hibler (1980) (HI80) and Lipscomb et al. (2007) (LI07). From our results and discussions, we can summarize the following conclusions:

- The ITD from the DEM simulations shows a significantly different shape compared to the ITD from the other three models, because HiDEM forms trapezoidal-shaped ridges, which the others do not (Fig. 4). The trapezoidal-shaped ridges cause a pronounced bump towards the thicker ice categories (Fig. 4).
- Implementing an ITD with a sub-grid parametrization of ridging seems to be beneficial for the representation of thick ice, as shown by the comparison of ITDs stemming from neXtSIM, using a mean thickness, and the redistribution schemes (HI80 and LI07) (Fig. 5).
- The shape of the ITD is sensitive to the spatial resolution of the ice thickness field from which the ITD is calculated (Fig. 9).
- We present an analytical redistribution function that captures the effect of triangular and trapezoidal ridge shapes. The main parameters in this function are the mean maximum keel depth and its standard deviation, and a tuning parameter governing the fraction of trapezoidal to triangular ridges (Eq. 1 and Fig. 8).

While the discrete-element-method simulations in this paper described a fairly simple deformation scenario, they still yield a deformed ice field with diverse ridge shapes and sizes. Thus, interesting next steps would be to study the effects of more complex forcing and to investigate ITDs related to shear-ridge formation, or start the simulations with an already deformed and partially healed ice cover.

Appendix A: Processing of HiDEM data

The standard simulation output of HiDEM contains information at the particle level, which needs to be transformed into gridded data to be comparable between HiDEM simulations and with neXtSIM. Particle level means that at every output timestep we know the location of each individual particle, but, for example, not the extent of a ridge consisting of several particles.

The gridded HiDEM data contains the ice thickness h as well as keel depth and sail height. To create the gridded data, the simulation domain is divided into a regular grid with the spacing dx depending on the initial ice thickness h_i, being the diameter of each particle, $dx = 4h_\mathrm{i}$. The ice thickness within each grid cell is calculated based on the minimum and maximum location of the centroid of each particle:

$h = z_{\max} + 0.5h_\mathrm{i} - (z_{\min} - 0.5h_\mathrm{i})$. Similarly, the keel depth and sail height are calculated, but with respect to the water level. Here, these calculations result in gridded data with a spatial resolution of 2 to 8 m.

It is important to note that the ice thickness calculated in areas with deformation contains the void space, macroporosity, between ice blocks in the ridges. This characteristic makes HiDEM the only model in this study to consider macroporosity, as opposed to neXtSIM and both redistribution models.

Appendix B: Sea-ice redistribution theory

Originally, the sea-ice redistribution was introduced by Thorndike et al. (1975) and then further developed by Lipscomb et al. (2007) to enhance model stability and improve agreement between modeled and observed ice thickness distributions.

In our case, the redistribution function Ψ only needs to be applicable for convergence. Thus, it can be described by the ridging mode w_r and the strain rate magnitude $|\dot{\epsilon}|$:

$$\Psi = w_r(h, g)|\dot{\epsilon}|. \tag{B1}$$

Similar to von Albedyll et al. (2022), we use the area change Δ as a proxy for $|\dot{\epsilon}|$ as we know how much area is added per time step dt to the system ($\Delta = 2Lvdt$ with L the length of the observation area in y-direction and v the ice velocity) and thus, needs to ridge to be comparable to the other simulations.

The ridging mode w_r is a function of the participation function $a(h)$, describing which ice gets ridged per thickness category h, and the distribution of ridged ice $n(h)$, and can be written as:

$$w_\mathrm{r} = \frac{-a(h) + n(h)}{N} \tag{B2}$$

N serves as a normalization factor for area conversation. The participation function is thus a function of $g(h)$, the original ITD:

$$a(h) = b(h)g(h). \tag{B3}$$

Here, we use the weighing function $b(h)$ introduced by Lipscomb et al. (2007), which is a smooth approximation of $b(h)$ originally formulated by Thorndike et al. (1975).

$$b(h) = \frac{e^{G(h)/a^*}}{a^* \cdot (1 - e^{-1/a^*})} \tag{B4}$$

with the empirical parameter $a^* = 0.05$ and the cumulative thickness distribution function $G(h)$. Thus, $b(h)$ allows all ice to participate in ridging, but favors the thin ice present. We only use one participation function, as the focus of this study lies on ridging.

Additionally, $n(h)$ depends on $a(h)$ and the ridging function $\gamma(h_\mathrm{i}, h)$

$$n(h) = \int_0^\infty a(h_\mathrm{i})\gamma(h_\mathrm{i}, h)\mathrm{d}h_\mathrm{i}, \tag{B5}$$

where h_i describes the initial thickness before ridging.

For $\gamma(h_\mathrm{i}, h)$ we implemented two different functions, which each are based on different redistribution approaches. Based on the geometrical assumption that the cross-section of a ridge is roughly triangular, Hibler (1980) (HI80) proposed a uniform distribution:

$$\gamma(h_\mathrm{i}, h) = \begin{cases} \frac{1}{2(H_* - h_\mathrm{i})}, & 2h_\mathrm{i} \le h \le 2\sqrt{H_* h_\mathrm{i}} \\ 0, & \text{otherwise} \end{cases} \tag{B6}$$

with the empirical thickness H_* influencing the maximum ice thickness of deformed ice. Thus, redistribution is only allowed between $2h_\mathrm{i}$ (rafting) and a limit depth for ridges $k_\mathrm{lim} = 2\sqrt{H_* h_\mathrm{i}}$. Later, Lipscomb et al. (2007) (LI07) developed an exponential function of γ

$$\gamma(h_\mathrm{i}, h) = \begin{cases} \gamma_0 e^{\frac{-(h - h_\mathrm{min})}{\mu\sqrt{h_\mathrm{i}}}}, & h \ge h_\mathrm{min} \\ 0, & \text{otherwise} \end{cases} \tag{B7}$$

with γ_0 being a normalization factor and μ a tunable parameter influencing the folding scale. The minimum thickness of ice participating in ridging h_min is defined as $h_\mathrm{min} = \min(2h_\mathrm{i}, h_\mathrm{i} + h_\mathrm{raft})$ with h_raft being 1 m.

Appendix C: Variability of the simulations

Both neXtSIM and HiDEM simulations were repeated five times for each initial ice thickness h_i. Thus, here we briefly describe the variability between these simulations regarding the spatial distribution of ridges as well as the resulting ice thickness distribution (ITD) and show that five simulations are representative of each simulation setup.

The deformed ice cover after $t = 2$ h for all neXtSIM simulations is shown in Fig. C1. All simulations show ridges forming a X-shape with smaller ridges developing seemingly from this main feature. In several simulations one arm of the X-shape is deeper and more localized, especially for $h_\mathrm{i} = 0.5$ and $h_\mathrm{i} = 1.0$ m, while the location of the ridges varies across the simulations. Nevertheless, the resulting ITDs (Fig. C2) from these simulations are virtually identical.

The deformed ice cover after $t = 2$ h for all HiDEM simulations is shown in Fig. C3. The general pattern of ridges in HiDEM is very similar across all HiDEM simulations, with the ridges being mainly perpendicular to the initial velocity. For $h_\mathrm{i} = 0.5$ and $h_\mathrm{i} = 1.0$ m, the wider ridges are around the edges of the observation area, while the interior features narrower ridges. Again, the exact location of ridges varies between all simulations. The thick ice ($h_\mathrm{i} = 2.0$ m) shows the

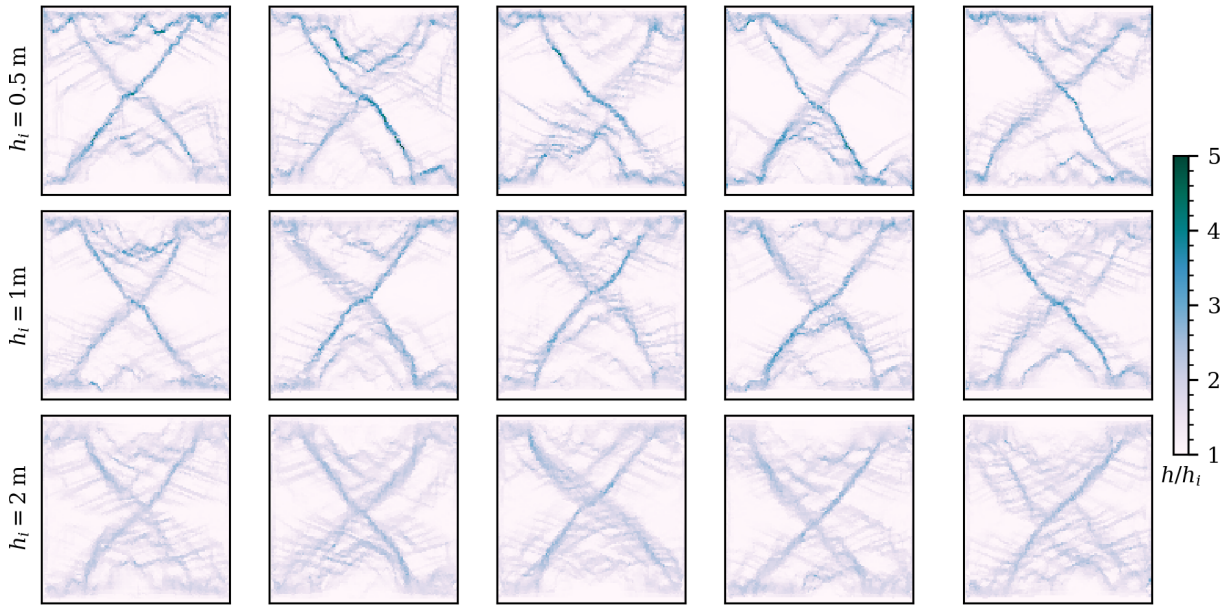


Figure C1. The final deformed ice cover ($t = 2$ h) from neXtSIM shown with the ice thickness h normalized by the initial thickness h_i. Each row shows the five different simulations for each initial ice thickness h_i (0.5, 1 and 2 m).

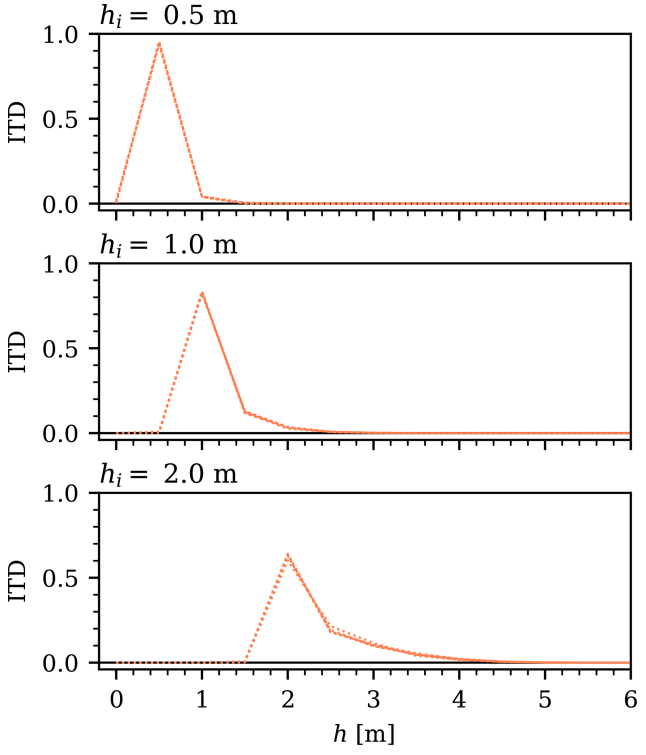


Figure C2. The ITD from the final deformed ice cover ($t = 2$ h) from neXtSIM shown for each individual simulation as a dashed line for each initial ice thickness h_i (0.5, 1 and 2 m).

largest variation in the ITD between the simulations (Fig. C4, with the variation being mainly in that some simulations only have one mode in the bump, while some other simulations have two modes, resulting in an overall flatter distribution of ridged ice. This variability is likely connected to variations in the depth of the plateau-area of the trapezoidal ridges. Thus, on the one hand, the depth of the ridges is not uniform, and, on the other hand, the plateau itself has some depth variation (Fig. 3). It is also likely that the variability between the ITDs is an effect of the size of the observation area as the observation area mainly features one large ridge for $h_\mathrm{i} = 2.0$ m (Fig. C3), while the ITDs for $h_\mathrm{i} = 0.5$ and $h_\mathrm{i} = 1.0$ m are virtually identical and are calculated from areas featuring several ridges.

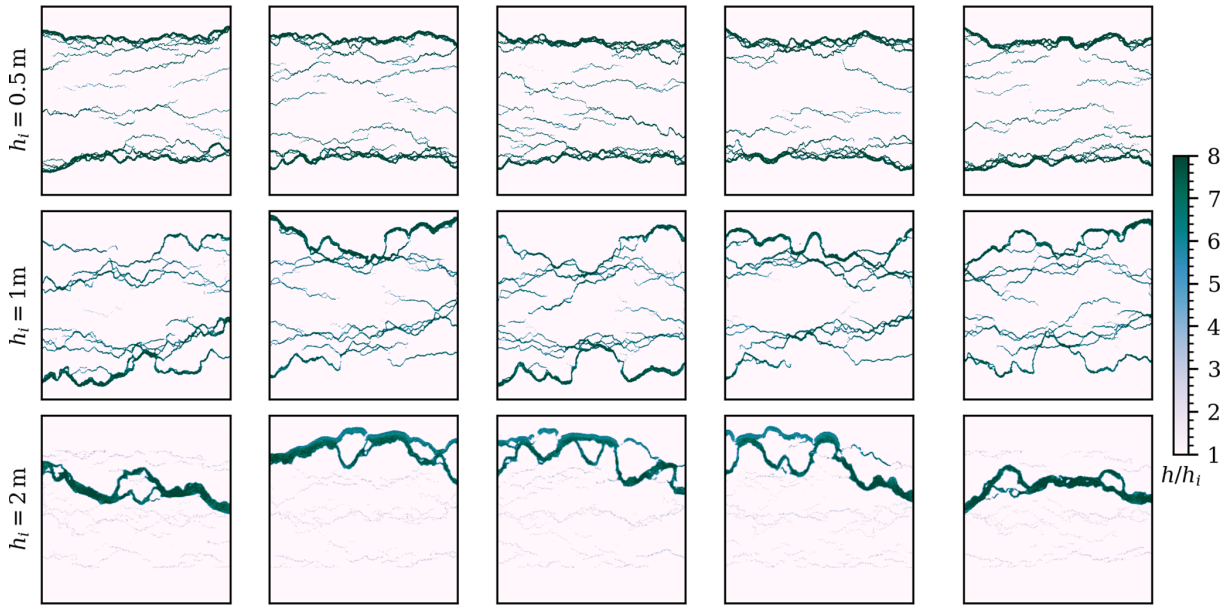


Figure C3. The final deformed ice cover ($t = 2$ h) from HiDEM shown with the ice thickness h normalized by the initial thickness h_i. Each row shows the five different simulations for each initial ice thickness h_i (0.5, 1 and 2 m).

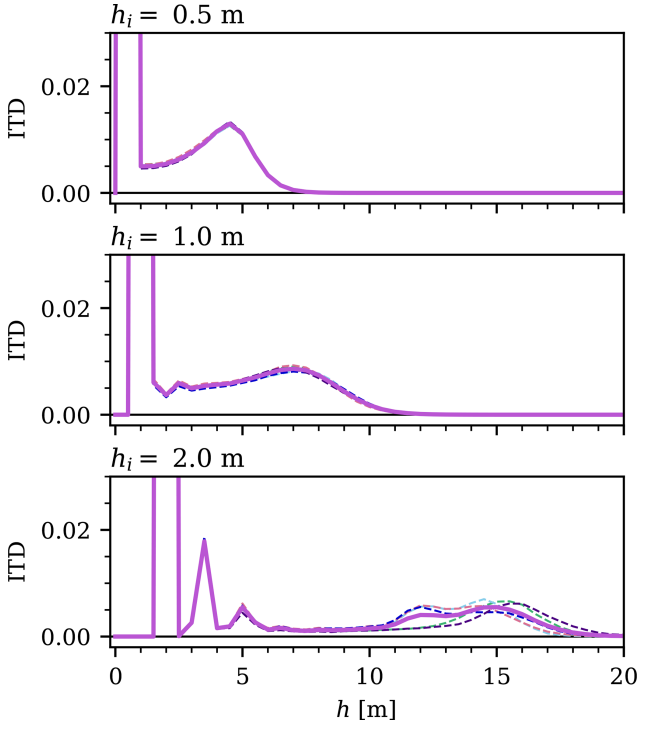


Figure C4. The ITD from the final deformed ice cover ($t = 2$ h) from HiDEM for each initial ice thickness h_i (0.5, 1 and 2 m). Each individual simulation is shown as a dashed line, while the mean is given as a solid line.

Appendix D: Derivation of $n(h)$

This section details the derivation of the distribution of ridged ice $n(h)$. This derivation is done with $n(h)$ respective to the sea-ice area covered by ridged ice. The distribution of ridged ice respective to the sea-ice volume $n_V(h)$ can then be calculated with $n_V(h) = n(h)h$, as continuum models typically feature $g(h)$ both for the sea-ice area and volume. Overall, the derivation of $n(h)$ is based on the idea that $n(h)$ should account for both triangular and trapezoidal ridges; $n(h)$ is split into three phases as shown in Fig. 7. Phase I is only influenced by triangular ridges, while phase III is only influenced by trapezoidal ridges. Consequently, phase II is the transition phase between the other two phases and is influenced by both triangular and trapezoidal ridges.

The contribution of triangular ridges to $n(h)$ is given by $n_{\mathrm{tri}}(h)$. Phase I is given by the constant amplitude a_{tri}. The contribution to phase II is described by a linear decline between the end of phase I, given by the ice thickness category h_{PI}, and the end of phase II, given by the ice thickness category h_{PII}, to facilitate a smoother transition between phase I and phase III.

$$n_{\mathrm{tri}}(h) = \begin{cases} a_{\mathrm{tri}}, & h_{\mathrm{i}} \le h < h_{\mathrm{PI}} \\ -\frac{a_{\mathrm{tri}}}{h_{\mathrm{PI}} - h_{\mathrm{PII}}} h + \frac{a_{\mathrm{tri}}}{h_{\mathrm{PI}} - h_{\mathrm{PII}}} h_{\mathrm{PI}}, & h_{\mathrm{PI}} \le h < h_{\mathrm{PII}} \end{cases} \tag{D1}$$

The contribution of trapezoidal ridges to $n(h)$ is described by a Gaussian normal distribution with the amplitude a_{tra}:

$$n_{\mathrm{tra}}(h) = a_{\mathrm{tra}} \exp\left(-\frac{\left(h - \overline{k}_{\max}\right)^2}{2\sigma_k} \right). \tag{D2}$$

This contribution both influences phase II and phase III.

The boundary between phase I and phase II was defined as $h_{\mathrm{PI}} = \overline{k}_{\max} - 2\sigma_k$, as per definition of a Gaussian normal distribution around 97 % of the distribution are accounted for above $\mu - 2\sigma$, with μ and σ being the mean and standard deviation of the distribution. Thus, the limit of $\overline{k}_{\max} - 2\sigma_k$ is set so that most of the Gaussian function is included in $n(h)$. This assumption also justifies the approximation done in Eq. (D2). The boundary between phase II and III was ad hoc defined as $h_{\mathrm{PII}} = \overline{k}_{\max} - 0.5\sigma_k$ so that the transition between Part I and Part III is smooth and phase II is comparably short. Additionally, $\overline{k}_{\max}$ and σ_k were chosen as parameters influencing the boundaries, as they are already necessary input parameters for $n(h)$. Thus, $n(h)$ was defined with the following boundaries:

$$n(h) = \begin{cases} n_{\mathrm{tri}}(h) & h_{\mathrm{i}} \le h < \overline{k}_{\max} - 2\sigma_k \\ n_{\mathrm{tri}}(h) + n_{\mathrm{tra}}(h) & \overline{k}_{\max} - 2\sigma_k \le h < \overline{k}_{\max} - 0.5\sigma_k \\ n_{\mathrm{tra}}(h) & \overline{k}_{\max} - 0.5\sigma_k \le h. \end{cases} \tag{D3}$$

The boundaries can then be applied to Eq. (D1) resulting in $n_{\mathrm{tri}}(h) = -\frac{a_{\mathrm{tri}}}{1.5\sigma_k} h + a_{\mathrm{tri}}\left(\overline{k}_{\max} - 0.5\sigma_k\right)$ for phase II.

To implement $n(h)$ both amplitudes, a_{tri} and a_{tra} need to be calculated. This calculation is based on the idea that the area under the curve of $n(h)$ can be described by the area of deformed ice A_{d}:

$$A_{\mathrm{d}} = A_{\mathrm{tri}} + A_{\mathrm{tra}} \tag{D4}$$

A_{tri} and A_{tra} are the triangular and trapezoidal contributions, respectively, to A_{d}. Additionally, the ratio of A_{tri} to A_{tra} is described by the tuning parameter α:

$$\frac{A_{\mathrm{tri}}}{A_{\mathrm{tra}}} = \alpha, \tag{D5}$$

which regulates the relationship between triangular to trapezoidal ridges, and thus, a higher α results in a less pronounced bump, signaling more trapezoidal ridges. Additionally, $\alpha > 0$, as trapezoidal ridges also have a contribution to the plateau of $n(h)$.

Both A_{tri} and A_{tra} can be calculated by integrating over the respective parts of $n(h)$. We integrate over $n_{\mathrm{tri}}(h)$ based on the boundaries given in Eq. (D3) to calculate A_{tri}:

$$A_{\mathrm{tri}} = \int_{h_{\mathrm{i}}}^{\overline{k}_{\max} - 2\sigma_k} a_{\mathrm{tri}} \, \mathrm{d}h + \int_{\overline{k}_{\max} - 2\sigma_k}^{\overline{k}_{\max} - 0.5} \left(-\frac{a_{\mathrm{tri}}}{1.5\sigma_k} h + a_{\mathrm{tri}}\left(\overline{k}_{\max} - 0.5\sigma_k\right) \right) \mathrm{d}h \tag{D6}$$

$$= a_{\mathrm{tri}}\left(\overline{k}_{\max} - h_{\mathrm{i}} - 1.25\sigma_k\right). \tag{D7}$$

Further, we calculate A_{tra} based on the integral of an arbitrary Gaussian function ($\int_{-\infty}^{\infty} \exp(-1(x+b)^2)\,\mathrm{d}x = \sqrt{\pi/a}$), while using the end of phase I as the lower boundary:

$$A_{\mathrm{tra}} = a_{\mathrm{tra}} \int_{h_{\mathrm{PI}}}^{\infty} \exp\left(-\frac{(h - \overline{k}_{\max})^2}{2\sigma_k}\right) \mathrm{d}h \approx a_{\mathrm{tra}} \sigma_k \sqrt{2\pi}. \tag{D8}$$

Now, the Eqs. (D4) and (D5) can be combined to

$$A_{\mathrm{d}} = A_{\mathrm{tri}} + A_{\mathrm{tra}} = A_{\mathrm{tri}}\left(1 + \frac{1}{\alpha}\right) \tag{D9}$$

$$A_{\mathrm{tra}} = A_{\mathrm{tri}}\left(\frac{1}{\alpha}\right) \tag{D10}$$

and the results from Eqs. (D6) and (D8) can be inserted, which results in a description of a_{tra} only depending on h_{i}, $\overline{k}_{\max}$ and σ_k:

$$a_{\mathrm{tra}} = \frac{a_{\mathrm{tri}}}{\alpha}\left(\frac{\overline{k}_{\max} - h_{\mathrm{i}} - 1.25\sigma_k}{\sigma_k \sqrt{2\pi}}\right). \tag{D11}$$

Implemented in the redistribution scheme, the workflow to calculate $n(h)$ is as follows. The amount of ice area A_{d}^t to

be deformed in the time step t is known and is added to A_d describing the overall amount of deformed ice present. Next, a_{tri} is calculated combining Eqs. (D6) and (D9):

$$a_{tri} = \frac{1}{A_d}\left(\bar{k}_{max} - h_i - 1.25\sigma_k\right)\left(1 + \frac{1}{\alpha}\right). \quad \text{(D12)}$$

The result of a_{tri} is then used to calculate a_{tra} based on Eq. (D11). Thus, all needed input parameters to calculate the resulting $n(h)$ are available and $n(h)$ can be updated.

Code and data availability. The HiDEM code used here is a beta-version and not yet publicly available, while an older released version of the code is available at Todd (2018). neXtSIM is generally available at https://github.com/nansencenter/nextsim (last access: 13 November 2026), while the exact version used for these experiments is archived at https://doi.org/10.5281/zenodo.17974261 (Ólason, 2025). The implementation of the sea-ice redistribution model and the analytical function and the simulation results can be requested from Marek Muchow.

Author contributions. MM, EÓ and AP conceptualized the study. EÓ adapted the neXtSIM to the study setup and MM created the HiDEM setup. MM conducted all simulations, analyzed the results, derived the analytical function and wrote the initial draft of the paper. EÓ and AP contributed to the analysis and writing of the paper. All authors contributed to the review of the paper.

Competing interests. The contact author has declared that none of the authors has any competing interests.

Disclaimer. Publisher's note: Copernicus Publications remains neutral with regard to jurisdictional claims made in the text, published maps, institutional affiliations, or any other geographical representation in this paper. The authors bear the ultimate responsibility for providing appropriate place names. Views expressed in the text are those of the authors and do not necessarily reflect the views of the publisher.

Acknowledgements. The authors wish to acknowledge CSC-IT Center for Science, Finland, for computational resources under the projects ESCARM: Extreme scale ice rheology modelling (grant no. 462000972). We sincerely thank the editor Qinghua Yang and two anonymous reviewers for their time, constructive feedback, and insightful comments.

Financial support. Marek Muchow was fundet by the AaltoENG 4-year doctoral program and acknowledges the funding from the European Union – NextGenerationEU instrument through Research Council of Finland under Grant (grant no. 348586) WindySea – "Modelling engine to design, assess environmental impacts, and operate wind farms for ice-covered waters". In addition, Marek Muchow was funded by the Finnish Maritime Foundation (Merenkulun Säätiö) for funding the research stay at the Nansen Center. Einar Ólason was supported by the MuSIC project, funded by the Norwegian Research Council (grant no. 325292) and internal funds from the Nansen Center. Arttu Polojärvi got financial support from the Research Council of Finland through the project (grant no. 347802) DEMFLO: Discrete Element Modeling of Continuous Ice Floes and Their Interaction.

Review statement. This paper was edited by Qinghua Yang and reviewed by two anonymous referees.

References

Amitrano, D., Grasso, J.-R., and Hantz, D.: From Diffuse to Localised Damage through Elastic Interaction, Geophys. Res. Lett., 26, 2109–2112, https://doi.org/10.1029/1999GL900388, 1999.

Amundrud, T. L., Melling, H., and Ingram, R. G.: Geometrical Constraints on the Evolution of Ridged Sea Ice, J. Geophys. Res.-Ocean., 109, https://doi.org/10.1029/2003jc002251, 2004.

Åström, J. and Polojärvi, A.: High-Resolution Fracture Dynamics Simulation of Pack-Ice and Drift-Ice Formation During Sea Ice Break up Events Using the HiDEM2.0 Code, Geophys. Res. Lett., 51, e2024GL110552, https://doi.org/10.1029/2024GL110552, 2024.

Åström, J., Robertsen, F., Haapala, J., Polojärvi, A., Uiboupin, R., and Maljutenko, I.: A Large-Scale High-Resolution Numerical Model for Sea-Ice Fragmentation Dynamics, The Cryosphere, 18, 2429–2442, https://doi.org/10.5194/tc-18-2429-2024, 2024.

Åström, J. A.: Statistical Models of Brittle Fragmentation, Adv. Phys., 55, 247–278, https://doi.org/10.1080/00018730600731907, 2006.

Blockley, E., Vancoppenolle, M., Hunke, E., Bitz, C., Feltham, D., Lemieux, J.-F., Losch, M., Maisonnave, E., Notz, D., Rampal, P., Tietsche, S., Tremblay, B., Turner, A., Massonnet, F., Ólason, E., Roberts, A., Aksenov, Y., Fichefet, T., Garric, G., Iovino, D., Madec, G., Rousset, C., y Melia, D. S., and Schroeder, D.: The Future of Sea Ice Modelling: Where Do We Go from Here? The Future of Sea Ice Modelling: Where Do We Go from Here?, Bull. Am. Meteorol. Soc., 101, E1304–E1311, https://doi.org/10.1175/bams-d-20-0073.1, 2020.

Bouchat, A., Hutter, N., Chanut, J., Dupont, F., Dukhovskoy, D., Garric, G., Lee, Y. J., Lemieux, J.-F., Lique, C., Losch, M., Maslowski, W., Myers, P. G., Ólason, E., Rampal, P., Rasmussen, T., Talandier, C., Tremblay, B., and Wang, Q.: Sea Ice Rheology Experiment (SIREx): 1. Scaling and Statistical Properties of Sea-Ice Deformation Fields, J. Geophys. Res.-Ocean., 127, https://doi.org/10.1029/2021jc017667, 2022.

Boutin, G., Ólason, E., Rampal, P., Regan, H., Lique, C., Talandier, C., Brodeau, L., and Ricker, R.: Arctic Sea Ice Mass Balance in a New Coupled Ice–Ocean Model Using a Brittle Rheology Framework, The Cryosphere, 17, 617–638, https://doi.org/10.5194/tc-17-617-2023, 2022.

Brenner, S., Rainville, L., Thomson, J., Cole, S., and Lee, C.: Comparing Observations and Parameterizations of Ice-Ocean Drag Through an Annual Cycle Across the Beaufort Sea, J. Geophys. Res.-Ocean., 126, e2020JC016977, https://doi.org/10.1029/2020JC016977, 2021.

Cundall, P. A. and Strack, O. D. L.: A Discrete Numerical Model for Granular Assemblies, Géotechnique, 29, 47–65, https://doi.org/10.1680/geot.1979.29.1.47, 1979.

Dansereau, V., Weiss, J., Saramito, P., and Lattes, P.: A Maxwell Elasto-Brittle Rheology for Sea Ice Modelling, The Cryosphere, 10, 1339–1359, https://doi.org/10.5194/tc-10-1339-2016, 2016.

Duncan, K. and Farrell, S. L.: Determining Variability in Arctic Sea Ice Pressure Ridge Topography With ICESat-2, Geophys. Res. Lett., 49, e2022GL100 272, https://doi.org/10.1029/2022GL100272, 2022.

Dupont, F., Dumont, D., Lemieux, J.-F., Dumas-Lefebvre, E., and Caya, A.: A Probabilistic Seabed–Ice Keel Interaction Model, The Cryosphere, 16, 1963–1977, https://doi.org/10.5194/tc-16-1963-2022, 2022.

Eilers, C. and Bradley, A.: Characteristic Geometry of Keels in Arctic Sea Ice Ridges, Geophys. Res. Lett., 53, e2025GL119003, https://doi.org/10.1029/2025GL119003, 2026.

Flato, G. M. and Hibler, W. D.: Ridging and Strength in Modeling the Thickness Distribution of Arctic Sea Ice, J. Geophys. Res.-Ocean., 100, 18611–18626, https://doi.org/10.1029/95JC02091, 1995.

Girard, L., Bouillon, S., Weiss, J., Amitrano, D., Fichefet, T., and Legat, V.: A New Modeling Framework for Sea-Ice Mechanics Based on Elasto-Brittle Rheology, Ann. Glaciol., 52, 123–132, https://doi.org/10.3189/172756411795931499, 2011.

Haas, C., Pfaffling, A., Hendricks, S., Rabenstein, L., Etienne, J.-L., and Rigor, I.: Reduced Ice Thickness in Arctic Transpolar Drift Favors Rapid Ice Retreat, Geophys. Res. Lett., 35, https://doi.org/10.1029/2008GL034457, 2008.

Haas, C., Lobach, J., Hendricks, S., Rabenstein, L., and Pfaffling, A.: Helicopter-Borne Measurements of Sea Ice Thickness, Using a Small and Lightweight, Digital EM System, J. Appl. Geophys., 67, 234–241, https://doi.org/10.1016/j.jappgeo.2008.05.005, 2009.

Herman, A.: Discrete-Element Bonded-Particle Sea Ice Model DESIgn, Version 1.3a – Model Description and Implementation, Geosci. Model Dev., 9, 1219–1241, https://doi.org/10.5194/gmd-9-1219-2016, 2016.

Hetenyi, M.: Beams on Elastic Foundation: Theory with Applications in the Fields of Civil and Mechanical Engineering, University of Michigan Press, 1946.

Hibler, W. D.: A Dynamic Thermodynamic Sea Ice Model, J. Phys. Oceanogr., 9, 815–846, https://doi.org/10.1175/1520-0485(1979)009<0815:adtsim>2.0.co;2, 1979.

Hibler, W. D.: Modeling a Variable Thickness Sea Ice Cover, Mon. Weather Rev., 108, 1943–1973, https://doi.org/10.1175/1520-0493(1980)108<1943:MAVTSI>2.0.CO;2, 1980.

Hopkins, M. A.: On the Ridging of Intact Lead Ice, J. Geophys. Res.-Ocean., 99, 16351–16360, https://doi.org/10.1029/94jc00996, 1994.

Hopkins, M. A.: The Effects of Individual Ridging Events on the Ice Thickness Distribution in the Arctic Ice Pack, Cold Reg. Sci. Technol., 24, 75–82, https://doi.org/10.1016/0165-232X(95)00006-W, 1996.

Hopkins, M. A.: Four Stages of Pressure Ridging, J. Geophys. Res.-Ocean., 103, 21883–21891, https://doi.org/10.1029/98jc01257, 1998.

Hopkins, M. A.: A Discrete Element Lagrangian Sea Ice Model, Eng. Comput., 21, 409–421, https://doi.org/10.1108/02644400410519857, 2004.

Hunke, E., Allard, R., Bailey, D. A., Blain, P., Craig, A., Dupont, F., DuVivier, A., Grumbine, R., Hebert, D., Holland, M., Jeffery, N., Lemieux, J.-F., Osinski, R., Rasmussen, T., Ribergaard, M., Roach, L., Roberts, A., Steketee, A., Turner, M., and Winton, M.: CICE-consortium/Icepack: Icepack 1.5.0, Zenodo, https://doi.org/10.5281/zenodo.14188409, 2024.

Hunke, E. C., Lipscomb, W. H., Turner, A. K., Jeffrey, N., and Elliott, S.: Cice: The Los Alamos Sea Ice Model Documentation and Software User's Manual Version 4.1 La-Cc-06-012, T-3 Fluid Dynamics Group, Los Alamos National Laboratory, 675, 500, https://doi.org/10.2172/1329842, 2010.

Hutter, N., Bouchat, A., Dupont, F., Dukhovskoy, D., Koldunov, N., Lee, Y. J., Lemieux, J.-F., Lique, C., Losch, M., Maslowski, W., Myers, P. G., Ólason, E., Rampal, P., Rasmussen, T., Talandier, C., Tremblay, B., and Wang, Q.: Sea Ice Rheology Experiment (SIREx): 2. Evaluating Linear Kinematic Features in High-Resolution Sea Ice Simulations, J. Geophys. Res.-Ocean., 127, https://doi.org/10.1029/2021jc017666, 2022.

Johnson, M., Proshutinsky, A., Aksenov, Y., Nguyen, A. T., Lindsay, R., Haas, C., Zhang, J., Diansky, N., Kwok, R., Maslowski, W., Häkkinen, S., Ashik, I., and de Cuevas, B.: Evaluation of Arctic Sea Ice Thickness Simulated by Arctic Ocean Model Intercomparison Project Models, J. Geophys. Res.-Ocean., 117, https://doi.org/10.1029/2011JC007257, 2012.

Krumpen, T., von Albedyll, L., Bünger, H. J., Castellani, G., Hartmann, J., Helm, V., Hendricks, S., Hutter, N., Landy, J. C., Lisovski, S., Lüpkes, C., Rohde, J., Suhrhoff, M., and Haas, C.: Smoother Sea Ice with Fewer Pressure Ridges in a More Dynamic Arctic, Nat. Clim. Change, 15, 66–72, https://doi.org/10.1038/s41558-024-02199-5, 2025.

Kulyakhtin and Høyland, K.: Distribution of Ice Block Sizes in Sails of Pressure Ice Ridges, in: The 22nd IAHR International Symposium on Ice, Proceedings of the 22nd IAHR International Symposium on Ice, 235–240, ISBN: 978-981-09-0750-1, 2014.

Lipscomb, W. H., Hunke, E. C., Maslowski, W., and Jakacki, J.: Ridging, Strength, and Stability in High-resolution Sea Ice Models, J. Geophys. Res.-Ocean., 112, https://doi.org/10.1029/2005jc003355, 2007.

Liu, C., Kulkarni, K., Suominen, M., Kujala, P., and Musharraf, M.: On the Data-Driven Investigation of Factors Affecting the Need for Icebreaker Assistance in Ice-Covered Waters, Cold Reg. Sci. Technol., 221, 104173, https://doi.org/10.1016/j.coldregions.2024.104173, 2024.

Mahoney, A., Eicken, H., and Shapiro, L.: How Fast Is Landfast Sea Ice? A Study of the Attachment and Detachment of Nearshore Ice at Barrow, Alaska, Cold Reg. Sci. Technol., 47, 233–255, https://doi.org/10.1016/j.coldregions.2006.09.005, 2007.

Manucharyan, G. E. and Montemuro, B. P.: SubZero: A Sea Ice Model With an Explicit Representation of the Floe Life Cycle, J. Adv. Model. Ea., 14, e2022MS003247, https://doi.org/10.1029/2022MS003247, 2022.

Mårtensson, S., Meier, H. E. M., Pemberton, P., and Haapala, J.: Ridged Sea Ice Characteristics in the Arctic from a Coupled Multicategory Sea Ice Model, J. Geophys. Res.-Ocean., 117, https://doi.org/10.1029/2010JC006936, 2012.

Martin, T., Tsamados, M., Schroeder, D., and Feltham, D. L.: The Impact of Variable Sea Ice Roughness on Changes in Arctic Ocean Surface Stress: A Model Study, J. Geophys. Res.-Ocean., 121, 1931–1952, https://doi.org/10.1002/2015JC011186, 2016.

Maus, S.: Bounds on the Initial Macroporosity of Sea Ice Pressure Ridges, Ann. Glaciol., 66, e10, https://doi.org/10.1017/aog.2025.4, 2025.

Maykut, G. A. and Untersteiner, N.: Some Results from a Time-Dependent Thermodynamic Model of Sea Ice, J. Geophys. Res., 76, 1550–1575, https://doi.org/10.1029/JC076i006p01550, 1971.

Melling, H. and Riedel, D. A.: Development of Seasonal Pack Ice in the Beaufort Sea during the Winter of 1991–1992: A View from Below, J. Geophys. Res.-Ocean., 101, 11975–11991, https://doi.org/10.1029/96jc00284, 1996.

Metzger, A. T., Mahoney, A. R., and Roberts, A. F.: The Average Shape of Sea Ice Ridge Keels, Geophys. Res. Lett., 48, e2021GL095100, https://doi.org/10.1029/2021GL095100, 2021.

Muchow, M. and Polojärvi, A.: Three-Dimensional Discrete Element Simulations on Pressure Ridge Formation, The Cryosphere, 18, 4765–4774, https://doi.org/10.5194/tc-18-4765-2024, 2024.

Ólason, E.: neXtSIM with moving boundary, Zenodo [code], https://doi.org/10.5281/zenodo.17974261, 2025.

Ólason, E., Boutin, G., Korosov, A., Rampal, P., Williams, T., Kimmritz, M., Dansereau, V., and Samaké, A.: A New Brittle Rheology and Numerical Framework for Large-Scale Sea-Ice Models, J. Adv. Model. Ea., 14, https://doi.org/10.1029/2021ms002685, 2022.

Petty, A. A., Tsamados, M. C., Kurtz, N. T., Farrell, S. L., Newman, T., Harbeck, J. P., Feltham, D. L., and Richter-Menge, J. A.: Characterizing Arctic Sea Ice Topography Using High-Resolution IceBridge Data, The Cryosphere, 10, 1161–1179, https://doi.org/10.5194/tc-10-1161-2016, 2016.

Potyondy, D. O. and Cundall, P. A.: A Bonded-Particle Model for Rock, Int. J. Rock Mech. Min., 41, 1329–1364, https://doi.org/10.1016/j.ijrmms.2004.09.011, 2004.

Prasanna, M., Polojärvi, A., Wei, M., and Åström, J.: Modeling Ice Block Failure within Drift Ice and Ice Rubble, Phys. Rev. E, 105, 045001, https://doi.org/10.1103/physreve.105.045001, 2022.

Rabenstein, L., Hendricks, S., Martin, T., Pfaffhuber, A., and Haas, C.: Thickness and Surface-Properties of Different Sea-Ice Regimes within the Arctic Trans Polar Drift: Data from Summers 2001, 2004 and 2007, J. Geophys. Res.-Ocean., 115, https://doi.org/10.1029/2009JC005846, 2010.

Ringeisen, D., Losch, M., Tremblay, L. B., and Hutter, N.: Simulating Intersection Angles between Conjugate Faults in Sea Ice with Different Viscous–Plastic Rheologies, The Cryosphere, 13, 1167–1186, https://doi.org/10.5194/tc-13-1167-2019, 2019.

Ringeisen, D., Hutter, N., and von Albedyll, L.: Deformation Lines in Arctic Sea Ice: Intersection Angle Distribution and Mechanical Properties, The Cryosphere, 17, 4047–4061, https://doi.org/10.5194/tc-17-4047-2023, 2023.

Roberts, A. F., Hunke, E. C., Kamal, S. M., Lipscomb, W. H., Horvat, C., and Maslowski, W.: A Variational Method for Sea Ice Ridging in Earth System Models, J. Adv. Model. Ea., 11, 771–805, https://doi.org/10.1029/2018ms001395, 2019.

Salganik, E., Høyland, K. V., and Maus, S.: Consolidation of Fresh Ice Ridges for Different Scales, Cold Reg. Sci. Technol., 171, 102959, https://doi.org/10.1016/j.coldregions.2019.102959, 2020.

Sanderson, T. J. O.: Ice Mechanics and Risks to Offshore Structures, Kluwer Academic Publishers,Norwell, MA, 1988.

Strub-Klein, L. and Sudom, D.: A Comprehensive Analysis of the Morphology of First-Year Sea Ice Ridges, Cold Reg. Sci. Technol., 82, 94–109, https://doi.org/10.1016/j.coldregions.2012.05.014, 2012.

Sumata, H., de Steur, L., Divine, D. V., Granskog, M. A., and Gerland, S.: Regime Shift in Arctic Ocean Sea Ice Thickness, Nature, 615, 443–449, https://doi.org/10.1038/s41586-022-05686-x, 2023.

Thorndike, A. S., Rothrock, D. A., Maykut, G. A., and Colony, R.: The Thickness Distribution of Sea Ice, J. Geophys. Res., 80, 4501–4513, https://doi.org/10.1029/jc080i033p04501, 1975.

Timco, G. W. and Burden, R. P.: An Analysis of the Shapes of Sea Ice Ridges, Cold Reg. Sci. Technol., 25, 65–77, https://doi.org/10.1016/S0165-232X(96)00017-1, 1997.

Timco, G. W. and Weeks, W. F.: A Review of the Engineering Properties of Sea Ice, Cold Reg. Sci. Technol., 60, 107–129, https://doi.org/10.1016/j.coldregions.2009.10.003, 2010.

Todd, J.: Joeatodd/HiDEM: HiDEM v2.1.0, Zenodo [code], https://doi.org/10.5281/zenodo.1402603, 2018.

Tsamados, M., Feltham, D. L., Schroeder, D., Flocco, D., Farrell, S. L., Kurtz, N., Laxon, S. W., and Bacon, S.: Impact of Variable Atmospheric and Oceanic Form Drag on Simulations of Arctic Sea Ice, J. Phys. Oceanogr., 44, https://doi.org/10.1175/JPO-D-13-0215.1, 2014.

Tuhkuri, J. and Lensu, M.: Laboratory Tests on Ridging and Rafting of Ice Sheets, J. Geophys. Res.-Ocean., 107, 8-1–8-14, https://doi.org/10.1029/2001jc000848, 2002.

Uusinoka, M., Haapala, J., Åström, J., Lensu, M., and Polojärvi, A.: Scale invariance in kilometer-scale sea ice deformation, EGUsphere [preprint], https://doi.org/10.5194/egusphere-2025-311, 2025a.

Uusinoka, M., Savard, A., Åström, J., Haapala, J., and Polojärvi, A.: Threshold Domain Sizes for Multifractality in Sea Ice Deformation, Geophys. Res. Lett., 52, e2025GL116833, https://doi.org/10.1029/2025GL116833, 2025b.

Valdez Banda, O. A., Goerlandt, F., Montewka, J., and Kujala, P.: A Risk Analysis of Winter Navigation in Finnish Sea Areas, Accident Anal. Prev., 79, 100–116, https://doi.org/10.1016/j.aap.2015.03.024, 2015.

von Albedyll, L., Haas, C., and Dierking, W.: Linking Sea Ice Deformation to Ice Thickness Redistribution Using High-Resolution Satellite and Airborne Observations, The Cryosphere, 15, 2167–2186, https://doi.org/10.5194/tc-15-2167-2021, 2021.

von Albedyll, L., Hendricks, S., Grodofzig, R., Krumpen, T., Arndt, S., Belter, H. J., Birnbaum, G., Cheng, B., Hoppmann, M., Hutchings, J., Itkin, P., Lei, R., Nicolaus, M., Ricker, R., Rohde, J., Suhrhoff, M., Timofeeva, A., Watkins, D., Webster, M., and Haas, C.: Thermodynamic and Dynamic Contributions to Seasonal Arctic Sea Ice Thickness Distributions from Airborne Observations, Elementa, 10, https://doi.org/10.1525/elementa.2021.00074, 2022.

Wadhams, P.: Sea Ice Thickness Distribution in the Greenland Sea and Eurasian Basin, May 1987, J. Geophys. Res.-Ocean., 97, 5331–5348, https://doi.org/10.1029/91JC03137, 1992.

West, B., O'Connor, D., Parno, M., Krackow, M., and Polashenski, C.: Bonded Discrete Element Simulations of Sea Ice With Non-Local Failure: Applications to Nares Strait, J. Adv. Model. Ea., 14, e2021MS002614, https://doi.org/10.1029/2021MS002614, 2022.

Wilchinsky, A. V., Feltham, D. L., and Hopkins, M. A.: Effect of Shear Rupture on Aggregate Scale Formation in Sea Ice, J. Geophys. Res.-Ocean., 115, https://doi.org/10.1029/2009JC006043, 2010.

Williams, T., Korosov, A., Rampal, P., and Ólason, E.: Presentation and Evaluation of the Arctic Sea Ice Forecasting System neXtSIM-F, The Cryosphere, 15, 3207–3227, https://doi.org/10.5194/tc-15-3207-2021, 2021.

Yu, Y., Maykut, G. A., and Rothrock, D. A.: Changes in the Thickness Distribution of Arctic Sea Ice between 1958–1970 and 1993–1997, J. Geophys. Res.-Ocean., 109, https://doi.org/10.1029/2003JC001982, 2004.